



## Disentangling the Components of the Milky Way

Inferring the Structure of the Milky Way in Phase-Space Using Gaussian Mixture  
Modelling with Extreme Deconvolution

A REPORT PRESENTED  
BY  
RAUNAQ RAI

### Departments

Department of Physics (Cavendish Laboratory)  
Institute of Astronomy

### Degree

MPhil in Data Intensive Science

### Supervision

Dr Anke Arentsen



St Edmund's College  
University of Cambridge

29th June 2025

## **Abstract**

# Contents

<b>1</b>	<b>Introduction</b>	<b>6</b>
1.1	Components of the Milky Way . . . . .	6
1.2	Metallicity as a Cosmic Clock . . . . .	6
1.3	$\Lambda$ CDM Model . . . . .	7
1.4	Accretion versus <i>in-situ</i> disc formation . . . . .	7
1.5	Origins of very-metal-poor disc candidates . . . . .	8
1.6	This Work . . . . .	8
<b>2</b>	<b>Data</b>	<b>9</b>
2.1	Sample construction . . . . .	9
2.2	Galactocentric Positions and Velocities . . . . .	9
<b>3</b>	<b>Methodology</b>	<b>12</b>
3.1	Gaussian Mixture Model . . . . .	12
3.2	Number of Gaussian Components . . . . .	13
<b>4</b>	<b>Results</b>	<b>14</b>
4.1	Gaussian Mixture Model Fit . . . . .	14
4.2	Rotational Support and the Onset of Disc Formation . . . . .	16
4.3	Residual Analysis for Hidden Disc Populations . . . . .	16
<b>5</b>	<b>Extension analysis</b>	<b>18</b>
5.1	Alpha-element abundance . . . . .	18
5.2	Data . . . . .	19
5.3	Gaussian Mixture Model Fit . . . . .	24
5.4	High alpha Gaussian Mixture Model Fit . . . . .	25
5.5	Low alpha Gaussian Mixture Model Fit . . . . .	26
5.6	Contrasting the high and low $\alpha$ GMMs . . . . .	26
<b>6</b>	<b>Discussion</b>	<b>27</b>
6.1	Reproducability of <a href="#">Zhang et al. [2024]</a> . . . . .	27
6.2	Expansion of <a href="#">Viswanathan et al. [2024]</a> . . . . .	28
6.3	Selection Effects and . . . . .	29
6.4	Limitations of GMM . . . . .	29
<b>7</b>	<b>Conclusion</b>	<b>30</b>

## List of Figures

- |   |  |    |
|---|--|----|
| 1 | Properties of the final RGB sample after all quality and footprint cuts. <i>Left</i> : heliocentric-distance histogram for the whole sample (grey); the subsets with $-3 < [\text{M}/\text{H}] < -1$ and $-3 < [\text{M}/\text{H}] < -2$ are shown in solid red and dashed blue, respectively. <i>Middle</i> : density map in Galactocentric cylindrical coordinates. The empty band at low $ Z $ is a selection artefact of our latitude/extinction cuts, which deliberately remove the thin-disc mid-plane; the concentration around $R \simeq 5\text{--}8\,\text{kpc}$ reflects the volume accessible to bright RGB stars interior to the Solar circle and coincides with the molecular ring region where the stellar surface density peaks. <i>Right</i> : Metallicity distribution of our data sample. Line colours are the same as in the left panel. (A reproduction of Figure 1 from <a href="#">Zhang et al. [2024]</a> ) . . . . . | 10 |
| 2 | Column-normalised density in the $v_\phi$ –[M/H] plane. <i>Left</i> : the bright-RGB catalogue of <a href="#">Andrae et al. [2023]</a> . <i>Right</i> : the same sample after all distance, dust, and quality cuts. Greyscale pixels show the normalised counts in each metallicity bin; the red dashed curve is the median $v_\phi$ , and the black curves trace the 16 <sup>th</sup> and 84 <sup>th</sup> percentiles. (A reproduction of Figure 2 from <a href="#">Zhang et al. [2024]</a> ) . . . . .  | 11 |
| 3 | Galactocentric velocity distributions as a function of metallicity. Each panel shows the column-normalised density of stars in the $v_R$ – $v_\phi$ plane for the metallicity interval printed at the top. With increasing metallicity the distribution contracts in both directions—signalling lower velocity dispersion—while the bulk of stars moves upward to larger prograde azimuthal velocity. (A reproduction of Figure 3 from <a href="#">Zhang et al. [2024]</a> ) . . . . .   | 11 |
| 4 | Ellipses mark the approximate extent of the thin disc (black), thick disc (grey), Gaia–Sausage/Enceladus debris (pink) and the pressure-supported stellar halo (purple). The figure serves as a visual key for interpreting the data panels in Fig. 3. . . . .   | 12 |
| 5 | BIC distributions as a function of the number of GMM components in each metallicity bin. The optimum number of components is indicated by the minimum BIC value (highlighted in red). (A reproduction of Figure 4 from <a href="#">Zhang et al. [2024]</a> ) . . . . .   | 13 |
| 6 | Gaussian Mixture Model decompositions of the stellar velocity distribution in the $v_R$ – $v_\phi$ plane for each metallicity bin. The bottom panel of each subfigure shows the 2D velocity distribution with GMM components overplotted as ellipses representing the $1\sigma$ contours in $v_R$ – $v_\phi$ . The top panel shows the fractional contribution. (A reproduction of Figure 5 from <a href="#">Zhang et al. [2024]</a> ) . . . . .   | 14 |
| 7 | Ratio of mean rotational velocity to azimuthal velocity dispersion, $V_{\text{rot}}/\sigma_\phi$ , for individual GMM components in each metallicity bin. Larger squares correspond to more dominant components. Colours match the GMM components in Figure 6.(A reproduction of Figure 6 from <a href="#">Zhang et al. [2024]</a> ) . . . . .   | 17 |

8	Top: Normalized residual maps between observed and GMM-predicted velocity distributions in $(v_R, v_\phi)$ for the VMP (left) and IMP (right) metallicity bins. Grey ellipses show the $2\sigma$ contour of the fiducial thick disc model. Bottom: Disc residuals as a function of injected disc fraction. The dashed line and blue band indicate the observed residual and its uncertainty. The solid black line and red region show mock test results and their uncertainties. (A reproduction of Figure 7 from <a href="#">Zhang et al. [2024]</a> )	18
9	Density of stars in the $[\alpha/M] - [M/H]$ plane. The high- $\alpha$ and low- $\alpha$ sequences are separated by the piece-wise linear boundary . The transition zone between the two sequences is clearly removed from this plot and discarded from subsequent analysis. (A reproduction of Figure 1 in <a href="#">Viswanathan et al. [2024]</a> )	20
10	Mean $[M/H]$ colour-coded in the Galactocentric $R-z$ plane. <i>Top</i> : the complete $G < 16$ RGB sample. <i>Bottom left</i> : high- $\alpha$ stars; <i>bottom right</i> : low- $\alpha$ stars. The high- $\alpha$ population is more centrally concentrated and shows a shallower vertical metallicity gradient. (A reproduction of Figure 2 in <a href="#">Viswanathan et al. [2024]</a> )	21
11	Azimuthal velocity as a function of metallicity. Each panel shows the column-normalised density in the $[M/H]-v_\phi$ plane together with running medians (red dashed) and 16th/84th percentiles (black). Left: full RGB sample. Centre / right: chemically separated high- $\alpha$ and low- $\alpha$ subsamples. (A reproduction of Figure 3 in <a href="#">Viswanathan et al. [2024]</a> )	22
12	Distribution of stars in $v_R-v_\phi$ space across eight metallicity bins (increasing left to right, top to bottom) for the high- $\alpha$ population (top) and low- $\alpha$ population (bottom). The low- $\alpha$ stars are clearly more rotation-supported at high metallicities, while the high- $\alpha$ sample shows a broader velocity structure across all bins, consistent with thick-disc and halo populations.	23
13	BIC scores for different metallicity bins, grouped by high- and low- $\alpha$ populations.	24
14	XD-GMM decomposition of high- $\alpha$ giants in four metallicity bins. Grey ellipses mark the $1\sigma$ contours of each Gaussian component.	25
15	XD-GMM decomposition of low- $\alpha$ giants in four metallicity bins. Grey ellipses show the $1\sigma$ contours of every Gaussian component.	26

## List of Tables

1	Parameters of the Gaussian mixture model fittings in different metallicity bins. The unit for all velocity columns is $\text{km s}^{-1}$ . . . . .	15
2	Number of Gaussian Mixture components selected by the BIC for each metallicity bin, split by $\alpha$ -sequence. . . . .	24
3	GMM component weights and kinematics for the high- $\alpha$ sequence. Velocities are in $\text{km s}^{-1}$ . Weights indicate the fraction of stars per metallicity bin. . . . .	25
4	XD-GMM component weights and kinematics for the low- $\alpha$ sequence. Velocities are in $\text{km s}^{-1}$ . Weights are the fractional contribution of each component. . . . .	26

# 1 Introduction

The Milky Way Galaxy, host to our solar system, is a spiral galaxy with a centre located approximately 150 000 trillion miles (or 25 000 lightyears) from Earth. Its formation history is complex and remains an active area of research. Being embedded within the Milky Way means we can study it in greater detail than any external galaxy, testing models of galaxy formation with high-precision observational data. One of the central aims of Galactic Archaeology is to reconstruct the Milky Way’s assembly by examining the chemical compositions and dynamical properties of its stars.

In this project, we reproduce and extend the analysis of [Zhang et al. \[2024\]](#), who investigated a very metal-poor disc component in the Milky Way. Very metal poor stars, formed from an interstellar medium unpolluted by earlier generations of supernovae, are among the oldest relics in the Galaxy. Discovering them on disc-like orbits would challenge the conventional view that the disc formed later from already enriched gas [[Bland-Hawthorn and Gerhard, 2016](#)], implying instead an earlier onset of disc assembly. Using Gaia DR3, the study by [Zhang et al. \[2024\]](#) applied a Gaussian Mixture Model with Extreme Deconvolution to the velocity distributions of stars across metallicity bins, probing whether a coherent disc signal persists down to the lowest metallicities.

## 1.1 Components of the Milky Way

The Milky Way is commonly decomposed into four stellar components: a *thin disc*, a *thick disc*, a central *bulge/bar*, and a roughly spherical *halo* [[Bland-Hawthorn and Gerhard, 2016](#), [Helmi, 2020](#)]. The thin disc describes the majority of stars and most of the interstellar gas in the galaxy. Ongoing star formation is concentrated in the “molecular-gas ring” where young, metal-rich stars trace nearly circular, co-rotating orbits with low velocity dispersion ( $\sigma_\phi \simeq 20 \text{ km s}^{-1}$ ). Above the mid-plane lies the thick disc: an older ( $\gtrsim 8\text{--}10$  Gyr), moderately metal-poor population, a scale height of  $z_{\text{scale}} \approx 1 \text{ kpc}$ , and hotter kinematics ( $\sigma_z \simeq 40 \text{ km s}^{-1}$ ) while still retaining net prograde rotation. Inside  $R \lesssim 2 \text{ kpc}$ , the central bulge—partly bar-shaped—hosts both old, metal-rich stars and a younger, actively forming component; stellar motions there combine bar-driven streaming with high random velocities ( $\sigma \sim 100 \text{ km s}^{-1}$ ). Encasing all of these is the stellar halo, which contributes only a few per cent of the total stellar mass yet includes the Galaxy’s oldest, most metal-poor stars ( $[\text{Fe}/\text{H}] \lesssim -1.5$ ) on highly eccentric or even retrograde orbits. Its low density, rich substructure, and kinematics indicate an origin in the hierarchical accretion and tidal disruption of dwarf galaxies and globular clusters. Together, the spatial distribution, chemistry, and dynamics of these four components include clues to the Milky Way’s star-formation history and its sequence of merger events.

## 1.2 Metallicity as a Cosmic Clock

Precise ages for individual old stars are difficult to measure, so their chemical composition – most commonly the iron-to-hydrogen ratio,  $[\text{Fe}/\text{H}]$  – is used as a surrogate clock. Very metal-poor (VMP) stars must have formed before successive generations of Type II and Type Ia supernovae had substantially enriched the interstellar medium, and therefore have low  $[\text{Fe}/\text{H}]$  values. Metallicity is inferred spectroscopically by measuring the equivalent widths of metal absorption lines, particularly Fe I and the Ca II H and K lines at 396.8 nm and 393.4 nm, respectively. After correcting for stellar effective temperature and surface

gravity, the relative strengths of these lines yield elemental abundances [Gray, 2005]. Large surveys (for example APOGEE, GALAH, LAMOST, and the Gaia XP spectra) now provide such measurements for millions of stars, enabling empirical age–metallicity relations that link chemistry to stellar chronometry [e.g. Nordström et al., 2004, Haywood et al., 2013, Leung and Bovy, 2019, Anders et al., 2023]. These studies consistently show that stars with  $[\text{Fe}/\text{H}] \lesssim -1$  are typically older than  $\sim 10$  Gyr, making low-metallicity populations valuable probes of the Milky Way’s earliest disc-building epochs.

### 1.3 $\Lambda$ CDM Model

In the concordance  $\Lambda$ CDM model, galaxy-sized haloes assemble hierarchically: small dark-matter clumps form first and then merge to build larger structures. Cosmological  $N$ -body simulations show that the number of subhaloes of mass  $M$  follows  $dn/dM \propto M^{-1.9}$ . For a Milky-Way-sized halo, this implies that over the  $\sim 14$  Gyr lifetime of the Universe (i.e. a Hubble time), the halo experiences:

- $\sim 10^2$  **minor** accretion events with  $M_{\text{sub}} \lesssim 10^9 M_\odot$ , and
- a few **major** mergers with  $M_{\text{sub}} \gtrsim 10^{10} M_\odot$ .

Only a small fraction of dark-matter haloes form significant numbers of stars. Below a critical virial mass of  $M_{\text{vir}} \sim 10^{11} M_\odot$ , reionisation and stellar feedback strongly suppress the efficiency of star formation. As a result, the stellar-mass–halo-mass (SMHM) relation becomes steep at the low-mass end [Purcell et al., 2007, Bullock and Boylan-Kolchin, 2017]: most low-mass subhaloes remain effectively “dark”, while only a few relatively massive dwarfs produce observable stellar populations.

Thus, although the Milky Way has accreted hundreds of subhaloes over its history, just one or two of the most massive dwarf galaxies contribute the bulk of the stellar halo’s mass; the rest contribute primarily dark matter and dynamical substructure.

After accretion, dynamical friction causes the most massive satellites to sink deep into the Galactic potential. Their orbits become increasingly radial, and their stellar debris is dispersed throughout the inner halo. This debris retains coherent signatures—strong radial anisotropy, distinctive angular momenta, and chemically narrow abundance sequences [e.g. Helmi and Tim de Zeeuw, 2000]. As a result, the stellar halo is not a smooth, featureless spheroid but a fossil record of the Galaxy’s merger history: its inner regions are shaped predominantly by a few massive accretions (e.g. Gaia-Sausage/Enceladus), while the outer halo reflects contributions from many lower-mass mergers.

### 1.4 Accretion versus *in-situ* disc formation

Chemical and kinematic evidence confirms that the metal-poor halo is primarily accreted. The debris of the Gaia–Sausage/Enceladus (GSE) event, for instance, is traced by stars with  $-2 < [\text{Fe}/\text{H}] < -1$  and extreme orbital anisotropy ( $\beta \gtrsim 0.8$ ; Belokurov et al. 2018, Helmi et al. 2018). At  $[\text{Fe}/\text{H}] \lesssim -2$  an even broader mix of minor mergers emerges, erasing any global rotation signal [Lancaster et al., 2019, Bird et al., 2021].

Against this backdrop, a number of studies have uncovered stars in the range  $-2 < [\text{Fe}/\text{H}] < -1$  whose velocities resemble a disc: modest eccentricities and net prograde rotation [Norris et al., 1985, Chiba and Beers, 2000, Carollo et al., 2019, An and Beers,

2020]. Gaia has pushed this frontier to  $[\text{Fe}/\text{H}] < -2$  [Sestito et al., 2019, Venn et al., 2020, Cordoni et al., 2020, Mardini et al., 2022]. Whether these objects represent (i) an *in-situ* metal-poor disc or (ii) the spun-up debris of earlier mergers remains hotly debated.

## 1.5 Origins of very-metal-poor disc candidates

Three broad formation scenarios have been proposed:

1. **Early *in-situ* disc.** Stars form in a gas-rich disc before  $z \sim 4$ , and later migrate outward or are dynamically heated; such stars would share the chemistry of the proto-Galaxy.
2. **Proto-galactic building blocks.** VMP stars originate in several massive, gas-rich satellites accreted at high redshift; their debris is dragged into the disc plane as the gaseous disc settles [e.g. Sestito et al., 2020].
3. **Late, minor prograde mergers.** Low-mass satellites on aligned orbits are assimilated after the disc forms, depositing a thin layer of metal-poor stars that retain disc-like kinematics [Santistevan et al., 2021].

Cosmological simulations generally reproduce scenario 2, finding that early mergers dominate the VMP budget while a coherent disc does not appear until  $z \lesssim 2$  [Gurvich et al., 2023].

Observationally, Belokurov and Kravtsov [2022] identified *Aurora*, a kinematically hot, weakly rotating population with  $-2 \lesssim [\text{Fe}/\text{H}] \lesssim -1.3$ , arguing against an extremely early disc. Follow-up work shows Aurora to be centrally concentrated [Rix et al., 2022, Arentsen et al., 2020a,b], consistent with heated debris rather than a long-lived thin disc. Furthermore, secular processes such as bar–halo resonances can impart a modest prograde bias to halo stars, mimicking a disc signal [Dillamore et al., 2023].

## 1.6 This Work

By reproducing the work by Zhang et al. [2024], this study assesses the claim that the Milky Way hosts a very-metal-poor (VMP;  $[\text{Fe}/\text{H}] < -2$ ) stellar disc. Using the catalogue from Andrae et al. [2023], data set is drawn from Gaia DR3, which supplies six-dimensional phase-space coordinates—sky position, parallax-based distance, proper motions, and radial velocity—for each star, together with homogeneous metallicity and  $\alpha$ -element abundances from the Gaia XP pipeline. To disentangle kinematic sub-populations we model the full three-dimensional velocity distribution  $(v_R, v_\phi, v_z)$  with a Gaussian Mixture Model, in successive narrow metallicity bins, whose parameters are inferred via Extreme Deconvolution (XD). The XD formalism explicitly folds the individual distance and proper-motion uncertainties into the likelihood, ensuring that measurement noise does not bias the recovered velocity values.

Astrophysically, a genuine disc should manifest itself as a high-weight Gaussian centred near the Local Standard of Rest ( $v_\phi \simeq 220 \text{ km s}^{-1}$ ) with small tangential and vertical dispersions ( $\sigma_\phi, \sigma_z \lesssim 30 \text{ km s}^{-1}$ ) and negligible mean radial motion, whereas the halo or any heated component should appear as a broad, almost isotropic Gaussian with little net rotation and dispersions of order  $120\text{--}150 \text{ km s}^{-1}$ . By tracking how the weight of the

cold, rotating component varies with metallicity we can determine when ordered rotation first emerged and test whether VMP stars were formed in situ or accreted from a satellite.

## 2 Data

### 2.1 Sample construction

Our catalogue is the bright ( $G < 16$ ) red-giant-branch sample of [Andrae et al. \[2023\]](#). Stellar metallicities are predicted with an Extreme Gradient Boosting model trained on high-resolution APOGEE DR17 spectra and a supplementary set of very metal-poor stars, ensuring reliable performance down to  $[M/H] \simeq -3.5$ . For each of the 17.6 million giants the catalogue contains values of  $[M/H]$ ,  $T_{\text{eff}}$ , and  $\log g$  with a random uncertainty of  $\simeq 0.1$  dex in  $[M/H]$  at  $G \lesssim 15$ . The catalogue only retains entries flagged as “high-confidence” and lying in  $-3.5 < [M/H] < +0.5$ .

Astrometric positions, proper motions, and radial velocities come from the main *Gaia* DR3 tables [[Gaia Collaboration et al., 2023](#)], while heliocentric distances are adopted from the Bayesian photo-geometric catalogue of [Bailer-Jones et al. \[2021\]](#). Because accurate velocities scale with distance precision, we impose a fractional-parallax-uncertainty cut  $\sigma_{\varpi}/\varpi < 0.10$  (FPU); stars that fail this threshold are discarded.

XP spectra are susceptible to reddening: heavy extinction dims the sources, lowers the XP signal-to-noise ratio, and biases the machine-learning metallicities. As in described [Zhang et al. \[2024\]](#), to minimise such systematics, stars with  $E(B-V)_{\text{SFD}} > 0.5$  or Galactic latitude  $|b| < 10^\circ$  were excluded. Colour-excess values from the SFD map accessed via dustmaps [[Green, 2018](#)] was used for this. These criteria remove regions where dust corrections are large and spatially variable, at the expense of a loss of sky coverage losing a large number of stars at low galactic latitudes.

Field-star kinematics can also be skewed by dense sub-structures. Accordingly, following [Zhang et al. \[2024\]](#), we remove all objects lying within  $1^\circ$  of any known globular cluster or dwarf-galaxy satellite using the list and data of these compiled by [Pace \[2024\]](#). This step removes obvious non-field populations (e.g. cluster members and recent accretion debris) without significantly reducing the statistical power of the sample.

After the metallicity flag, distance-quality, reddening, latitude, and sub-structure cuts, our working data set comprises  $\sim 3.4 \times 10^6$  red-giant stars possessing homogeneous metallicities and six-dimensional phase-space information.

### 2.2 Galactocentric Positions and Velocities

Six-dimensional phase-space coordinates are obtained with `astropy.coordinates`. We adopt a Galactocentric frame with  $R_0 = 8.1$  kpc and  $Z_0 = 25$  pc [[McMillan, 2016](#)], and a solar velocity<sup>1</sup>  $(U_\odot, V_\odot, W_\odot) = (11.1, 245, 7.25) \text{ km s}^{-1}$  [[Schönrich et al., 2010](#)]. The cylindrical velocity components  $(v_R, v_\phi, v_Z)$  are extracted from the transformed SkyCoord module.

---

<sup>1</sup>Cartesian components  $(U, V, W)$ , where  $U$  is radially outwards,  $V$  is aligned with Galactic rotation, and  $W$  points to the North Galactic Pole.

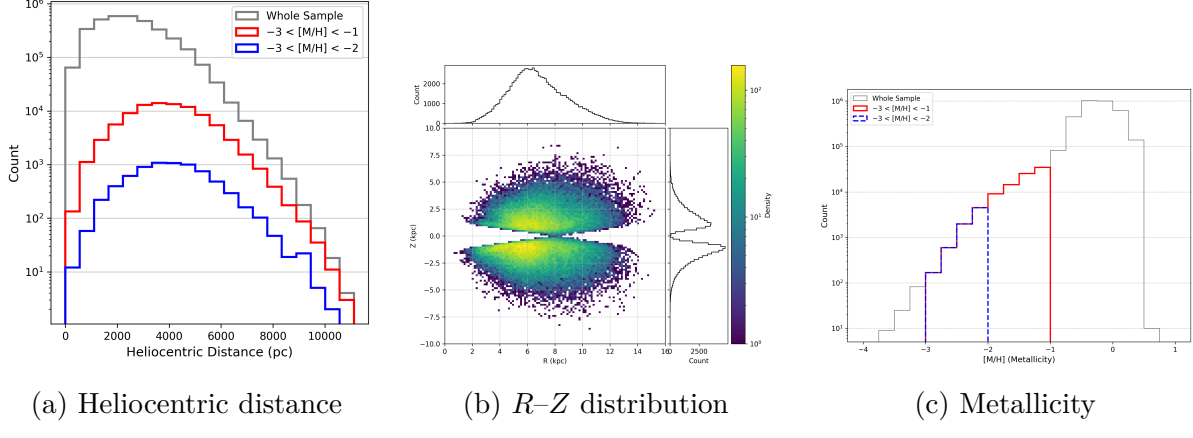


Figure 1: Properties of the final RGB sample after all quality and footprint cuts. *Left:* heliocentric-distance histogram for the whole sample (grey); the subsets with  $-3 < [\text{M}/\text{H}] < -1$  and  $-3 < [\text{M}/\text{H}] < -2$  are shown in solid red and dashed blue, respectively. *Middle:* density map in Galactocentric cylindrical coordinates. The empty band at low  $|Z|$  is a selection artefact of our latitude/extinction cuts, which deliberately remove the thin-disc mid-plane; the concentration around  $R \approx 5\text{--}8\text{ kpc}$  reflects the volume accessible to bright RGB stars interior to the Solar circle and coincides with the molecular ring region where the stellar surface density peaks. *Right:* Metallicity distribution of our data sample. Line colours are the same as in the left panel. (A reproduction of Figure 1 from [Zhang et al. \[2024\]](#))

To propagate measurement errors we generate  $N_{\text{MC}} = 100$  Monte-Carlo realisations per star, drawing parallax, proper motions, radial velocity, and distance from their reported uncertainties (the proper-motion covariance is honoured through a bivariate normal). Each realisation is transformed to the Galactocentric frame, yielding distributions of  $v_R$ ,  $v_\phi$ , and  $v_Z$ ; the  $1\sigma$  widths of those distributions are stored as per-star velocity uncertainties.

As shown in Figure 2, stellar azimuthal velocities evolve increase with metallicity. Halo-like kinematics dominate at  $[\text{M}/\text{H}] \lesssim -1.5$  with statistics indicative of a pressure-supported component. A rapid spin-up appears over the metallicity range  $[\text{M}/\text{H}] \simeq -1.3$  to  $-0.9$ , consistent with [Belokurov and Kravtsov \[2022\]](#). By  $[\text{M}/\text{H}] \gtrsim -0.5$  the stellar azimuthal velocities reaches the Local Standard-of-Rest value ( $\approx 220 \text{ km s}^{-1}$ ) and the velocity dispersion dispersion falls, marking the transition to a disc. Visually, using 2, we can observe that the onset of ordered rotation in the Milky Way occurred when the inter-stellar medium reached roughly one-tenth solar metallicity.

As shown in Fig. 3, stars with  $[\text{M}/\text{H}] \geq -1.0$  have a strong prograde bias in azimuthal velocities, with a peak at  $v_\phi \gtrsim 180 \text{ km s}^{-1}$  and a relatively narrow distribution in  $v_R$ . As shown in Fig. 4, this is consistent with the thin- and thick-disc ellipses. Below  $[\text{M}/\text{H}] \simeq -1.0$  the distribution broadens and drops toward  $v_\phi \approx 0$ , indicating pressure supported kinematics, characteristic of the stellar halo and the radial Gaia-Sausage/Enceladus debris. At the lowest metallicities ( $[\text{M}/\text{H}] \lesssim -1.5$ ) the contours are nearly isotropic with only a mild prograde bias. Hence, any rotation-supported very-metal-poor disc must contribute at most a small fraction of the population. In subsequent analysis we quantitatively assess these observations.

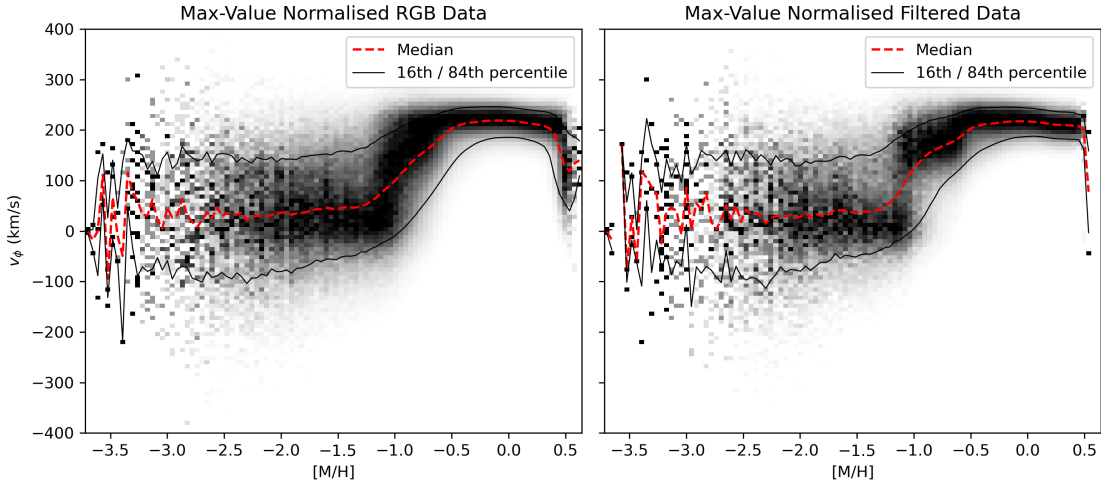


Figure 2: Column-normalised density in the  $v_\phi$ -[M/H] plane. *Left:* the bright-RGB catalogue of [Andrae et al. \[2023\]](#). *Right:* the same sample after all distance, dust, and quality cuts. Greyscale pixels show the normalised counts in each metallicity bin; the red dashed curve is the median  $v_\phi$ , and the black curves trace the 16<sup>th</sup> and 84<sup>th</sup> percentiles. (A reproduction of Figure 2 from [Zhang et al. \[2024\]](#))

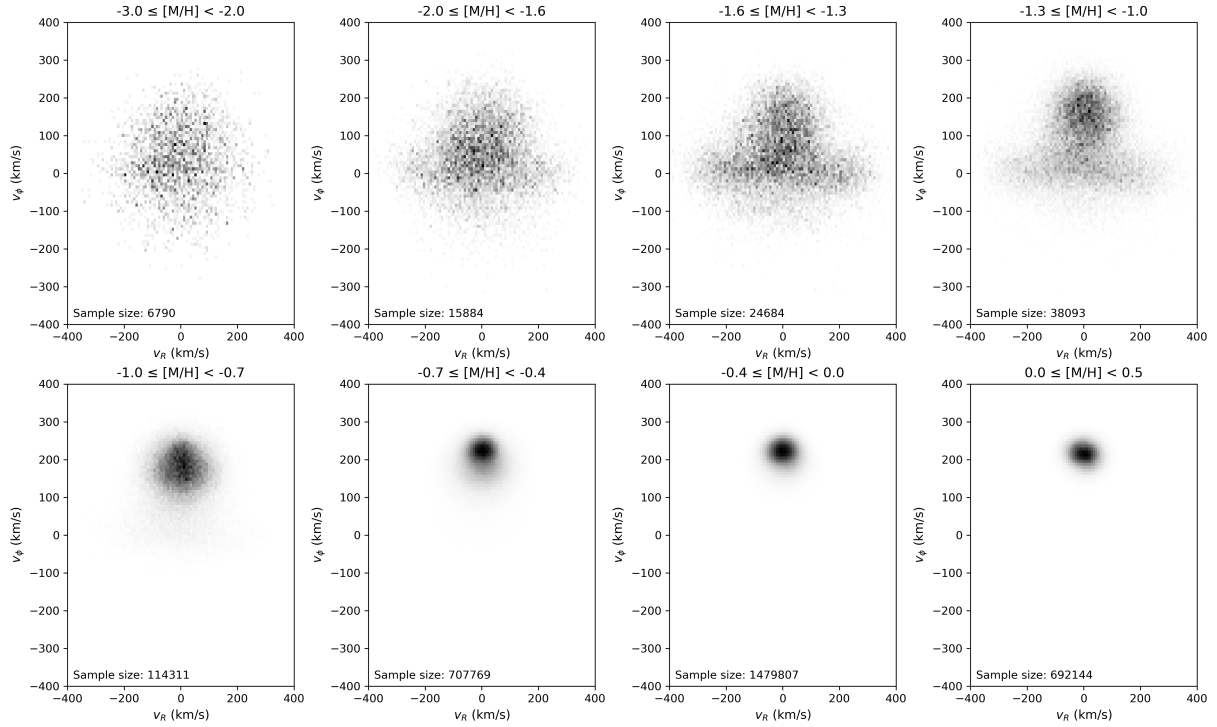


Figure 3: Galactocentric velocity distributions as a function of metallicity. Each panel shows the column-normalised density of stars in the  $v_R$ - $v_\phi$  plane for the metallicity interval printed at the top. With increasing metallicity the distribution contracts in both directions—signalling lower velocity dispersion—while the bulk of stars moves upward to larger prograde azimuthal velocity. (A reproduction of Figure 3 from [Zhang et al. \[2024\]](#))



Figure 4: Ellipses mark the approximate extent of the thin disc (black), thick disc (grey), Gaia–Sausage/Enceladus debris (pink) and the pressure-supported stellar halo (purple). The figure serves as a visual key for interpreting the data panels in Fig. 3.

Given we are testing whether a very-metal-poor stellar disc exists, we naturally restrict the sample to stars within  $|Z| < 2.5$  kpc of the galactic mid-plane. This keeps the focus on stars close to the plane, where any disc-like population (whether formed in situ or deposited by mergers) would be found [Tkachenko et al., 2025].

Upon comparison with Zhang et al. [2024], we note that our sample is approximately the same size - with a difference of less than 0.002% of the sample size in each bin.

### 3 Methodology

#### 3.1 Gaussian Mixture Model

To quantitatively investigate the kinematic structure of metal-poor stars and assess the presence of a potential very-metal-poor disc, we use a Gaussian Mixture Model (GMM) framework as done by Zhang et al. [2024]. GMMs are a class of unsupervised machine learning algorithms commonly used in data science for clustering and density estimation. They model a dataset as a weighted sum of multivariate Gaussian distributions, each corresponding to a latent sub-population within the data.

From a probabilistic perspective, the GMM assumes that each observed data point is generated from a hidden (latent) variable indicating membership in one of the Gaussian components. This latent space formulation allows the model to assign probabilistic classifications to data points, providing a soft clustering where each star has a fractional likelihood of belonging to each component. In our case, the data are three-dimensional velocity vectors  $(v_R, v_\phi, v_Z)$ , and the latent space captures distinct kinematic substructures in this space.

We implement the GMM fitting using the pyGMMis package [Melchior and Goulding, 2016] in the  $v_R$ ,  $v_\phi$ , and  $v_Z$  phase space. This algorithm extends the standard Expectation-Maximisation (EM) algorithm with the “Extreme Deconvolution” technique developed by Bovy et al. [2011]. This method is particularly well-suited to astronomical datasets, as it incorporates measurement uncertainties into the GMM fitting by modifying the EM updates to account for known errors on each data point. In our case, these uncertainties are derived from the Gaia astrometric and spectroscopic data and are represented by

diagonal covariance matrices encoding the squared uncertainties in  $v_R$ ,  $v_\phi$ , and  $v_Z$  for each star.

### 3.2 Number of Gaussian Components

We apply the GMM separately to each metallicity bin with  $[\text{M}/\text{H}] < -1$ , as we are specifically interested in detecting any rotationally supported structure among the very metal-poor stars. An important decision must be made when implementing the appropriate number of components in applying Gaussian Mixture Models. Too few components may underfit the data, missing real substructures, while too many will overfit, leading to spurious and physically uninterpretable results.

We select the optimal number of components using the Bayesian Information Criterion (BIC) [Schwarz 1978](#). The BIC is defined as

$$\text{BIC} = k \ln(n) - 2 \ln \mathcal{L}, \quad (1)$$

where  $k = (1 + 3 + 6) \times N - 1$  is the total number of free parameters in a model with  $N$  Gaussian components (accounting for the weights, means, and covariances),  $n$  is the number of stars in the sample, and  $\mathcal{L}$  is the maximum likelihood of the fit. The BIC penalizes model complexity, such that adding extra components without a significant gain in likelihood will result in a higher BIC value.

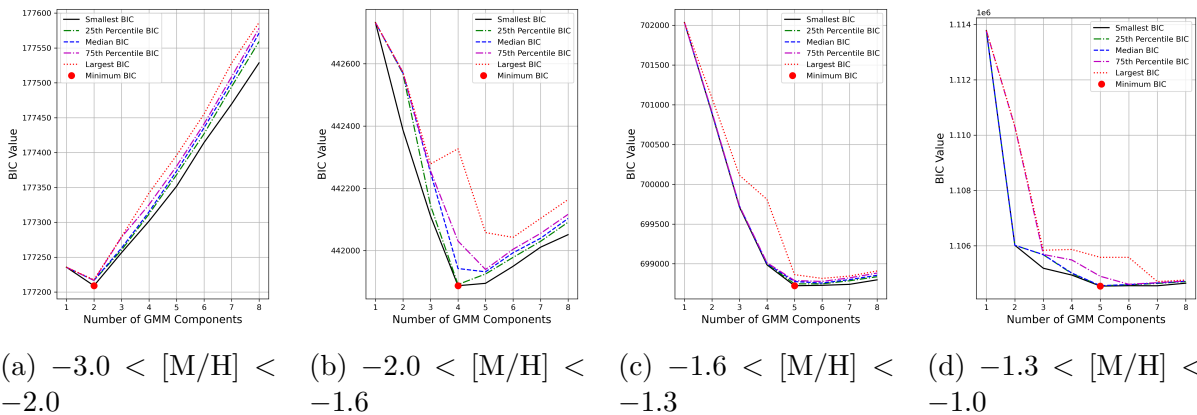


Figure 5: BIC distributions as a function of the number of GMM components in each metallicity bin. The optimum number of components is indicated by the minimum BIC value (highlighted in red). (A reproduction of Figure 4 from [Zhang et al. \[2024\]](#))

The Expectation-Maximisation algorithm can become trapped in local minima, so we performed 50 initialisations for each  $N$  and recorded the BIC value for each trial. The minimum BIC value across all trials indicated the statistically preferred model and suggests that the global optimum was likely reached.

To improve convergence and model stability, the GMM components in each trial were initialised using the kmeans algorithm. This is due to the sensitivity of GMMs to their starting conditions: poor initialisation can lead to convergence on undesirable solutions, particularly in high-dimensional or overlapping data. KMeans clustering provides an initialisation point by partitioning the velocity space into compact, roughly spherical

clusters. This works well with the assumptions of Gaussian components and often gives faster, more stable convergence and more physically meaningful results. In our application, where stellar substructures are partially overlapping in velocity space, this method applies well.

In Figure 5, we show the distribution of BIC values across four metallicity bins as a function of  $N$ . The resulting preferred number of components are 2, 4, 5, and 5 for the VMP, IMP, MP1, and MP2 bins. This is in agreement with the findings of [Zhang et al. \[2024\]](#). Our analysis, however, selects the lowest BIC each time, removing the need for a subjective choice of the number of components when BIC values are very similar. [Zhang et al. \[2024\]](#), when observing the BIC values for the MP1 bin chooses to use 5 components instead of 6 despite the BIC score for the 6-component model being lower than the 5-component model.

## 4 Results

### 4.1 Gaussian Mixture Model Fit

Using the number of components selected by the BIC criteria, we fit the GMM to the data in each metallicity bin as shown in Figure 6. We increased the number of initialisations to 100 for the final fitting to ensure convergence to a stable solution.

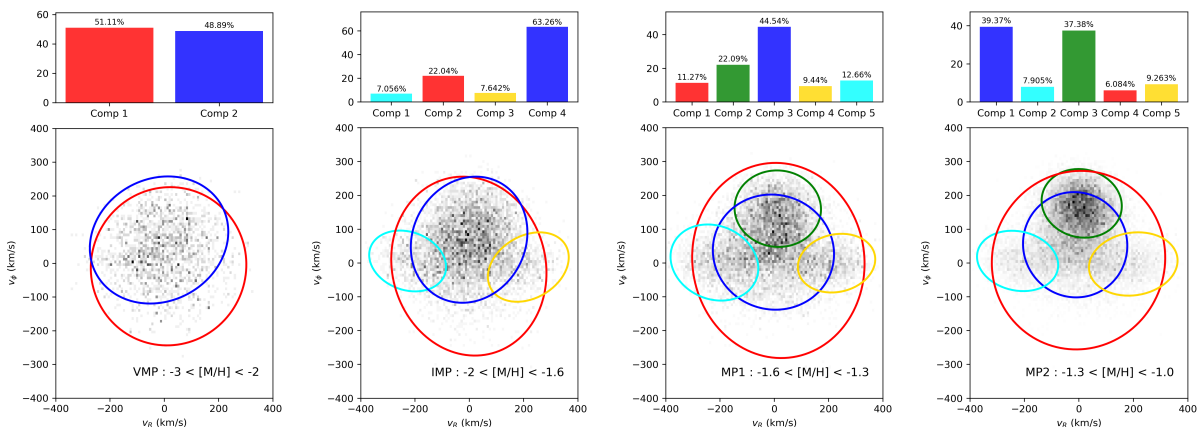


Figure 6: Gaussian Mixture Model decompositions of the stellar velocity distribution in the  $v_R$ - $v_\phi$  plane for each metallicity bin. The bottom panel of each subfigure shows the 2D velocity distribution with GMM components overplotted as ellipses representing the  $1\sigma$  contours in  $v_R$ - $v_\phi$ . The top panel shows the fractional contribution. (A reproduction of Figure 5 from [Zhang et al. \[2024\]](#))

As shown in Figure 6, the GMM is able to capture kinematic substructures in the velocity space of metal-poor stars. As metallicity increases, a gaussian component with a clear prograde rotation signal emerges (in green), indicative of a disc-like structure. The statistics of the GMM fit are summarised in Table 1, which lists the weights, means, and dispersions of each component in the four metallicity bins.

At  $[M/H] < -1.6$  (the VMP and IMP regimes), a disc component is not observed. Instead, the kinematic structure is dominated by a prograde halo and a stationary halo. In the VMP bin, the sample is almost evenly split between these two components, with

Components	Weights (%)	$v_R$	$\sigma_R$	$v_\phi$	$\sigma_\phi$	$v_Z$	$\sigma_Z$
<b>VMP:</b> $-3.0 < [\text{M}/\text{H}] < -2.0$ (4768 stars)							
Stationary halo	51.1	15.86	143.17	-9.13	117.36	-0.08	122.64
Prograde halo	48.9	-19.14	127.43	68.86	94.28	-0.90	82.89
<b>IMP:</b> $-2.0 < [\text{M}/\text{H}] < -1.6$ (12052 stars)							
Stationary halo	22.0	-1.45	142.88	-9.59	132.32	-0.91	124.92
Prograde halo	63.3	-0.58	107.32	68.52	93.27	-1.16	72.56
GS/E(1)	7.1	-226.92	70.78	5.60	44.98	8.43	88.40
GS/E(2)	7.6	217.52	74.41	-12.35	51.35	-4.22	89.78
<b>MP1:</b> $-1.6 < [\text{M}/\text{H}] < -1.3$ (19142 stars)							
Stationary halo	11.3	15.09	158.68	7.11	144.33	-2.55	132.08
Prograde halo	44.5	-3.02	111.54	31.79	85.15	-0.54	70.36
GS/E(1)	12.7	-220.40	80.76	1.01	56.29	0.47	91.00
GS/E(2)	9.4	229.32	71.22	-0.82	43.42	1.42	92.69
Thick disc	22.1	12.93	79.56	160.32	56.58	-2.31	68.83
<b>MP2:</b> $-1.3 < [\text{M}/\text{H}] < -1.0$ (30892 stars)							
Stationary halo	6.1	-1.17	159.06	8.07	132.05	-3.37	120.46
Prograde halo	39.4	-13.47	95.65	53.64	77.86	-3.04	71.00
GS/E(1)	7.9	-224.68	74.44	5.73	44.63	2.41	87.27
GS/E(2)	9.3	199.71	81.28	-3.30	46.84	-2.07	88.99
Thick disc	37.4	10.56	73.55	176.07	50.79	0.85	62.03

Table 1: Parameters of the Gaussian mixture model fittings in different metallicity bins. The unit for all velocity columns is  $\text{km s}^{-1}$ .

the stationary halo contributing 51.1% and the prograde halo 48.9%. Both show broad velocity dispersions, with only modest rotational support ( $\langle v_\phi \rangle \sim 69 \text{ km s}^{-1}$  for the prograde halo) and no evidence for a kinematically cold disc-like structure.

In the IMP bin, the picture remains qualitatively similar, although the prograde halo dominates more strongly (63.3%) and additional substructure becomes apparent. Two minor components, interpreted as fragments of the Gaia–Sausage/Enceladus (GS/E) merger debris, are also identified, each contributing  $\sim 7\%$  of the population and exhibiting highly radial orbits ( $|v_R| > 200 \text{ km s}^{-1}$ ). These GS/E components are characterised by strong anisotropy and contribute to the broadening of the halo distribution, but again show no signature of disc-like kinematics. The absence of a cold, rotating disc in these bins suggests that if a very-metal-poor disc exists, it must be a minor contributor to the local stellar population.

Our GMM decomposition recovers the same substructures identified by [Zhang et al. \[2024\]](#) across all metallicity bins. We find similar velocity dispersions and centroid trends for the stationary halo, prograde halo, and GS/E components. Notably, our model assigns a more comparable weight to the prograde halo component in the VMP bin, in contrast to the dominant stationary halo reported by [Zhang et al. \[2024\]](#). We also observe some variation in the centroid  $v_\phi$  values of GS/E substructures, although their bimodal spatial structure is preserved.

## 4.2 Rotational Support and the Onset of Disc Formation

To assess the degree of rotational support in each component, we compute the ratio  $V_{\text{rot}}/\sigma_\phi$ , where  $V_{\text{rot}}$  is the mean azimuthal velocity and  $\sigma_\phi$  its dispersion. This ratio serves as a conventional diagnostic of disc-like kinematics, with values  $\gtrsim 3$  indicating rotation-supported populations. As shown in Figure 7, all components in the VMP and IMP bins fall below this threshold, confirming that the GMM identifies only dynamically hot, dispersion-supported structures in these regimes. This is consistent with the interpretation of the dominant components as stationary and prograde halo populations, with  $V_{\text{rot}}/\sigma_\phi \approx 0.7$  in both cases (see also Table 1).

At higher metallicities, a dynamically colder disc population emerges. In the MP1 bin, the thick disc component (green) rotates at  $v_\phi \sim 160 \text{ km s}^{-1}$  with  $\sigma_\phi \sim 57 \text{ km s}^{-1}$ , yielding  $V_{\text{rot}}/\sigma_\phi \approx 2.8$ . While just below the canonical boundary, this component's low vertical dispersion and substantial weight (22.1%) mark it as a distinct disc-like structure. By the MP2 bin, the disc becomes the dominant component (37.4%), with  $V_{\text{rot}}/\sigma_\phi \approx 3.5$ , indicating clear rotational support and a well-established thick disc. These trends point to a sharp transition in the stellar kinematics around  $[\text{M}/\text{H}] \sim -1.5$ , consistent with the early onset of disc formation.

Meanwhile, the GS/E components — identifiable in the IMP, MP1, and MP2 bins — remain dynamically distinct, with high  $|v_R|$ , relatively small  $v_\phi$ , and negligible rotational support, reinforcing their origin as debris from a major radial merger [Helmi et al., 2018]. Notably, given the estimated time of the GS/E accretion event (of order 8–11 Gyr ago [Gallart et al., 2019, Belokurov et al., 2020, Di Matteo et al., 2019]), its stellar debris is expected to be phase-mixed. This implies that the positive and negative  $v_R$  components should contribute approximately equally. This symmetry is indeed observed in the two MP bins. However, in the IMP bin the distribution is clearly asymmetric, with the negative  $v_R$  GS/E component (aqua) containing nearly twice as many stars as the positive one (orange). This may suggest incomplete phase mixing or contamination by other structures at this intermediate metallicity.

## 4.3 Residual Analysis for Hidden Disc Populations

One of the limitations of GMMs is that they can fail to detect substructures that contribute only weakly to the overall distribution. To address this, we perform a residual analysis to test whether a disc-like population—too weak to be picked up by the GMM—might nonetheless be present in the VMP and IMP metallicity regimes.

We generated a synthetic dataset by drawing the same number of mock stars as observed stars from the best-fit GMM in each bin. Since our GMM uses the Extreme Deconvolution algorithm, which accounts for observational uncertainties during fitting, the raw samples from the model are noise-free. However, comparing these directly to real data would be inappropriate due to the absence of measurement error. To resolve this, we assign each mock star the velocity uncertainties of its nearest neighbour in the observed data (in  $(v_R, v_\phi, v_Z)$  space), and then add Gaussian noise according to these uncertainties.

We then bin both the observed and mock data in the  $(v_R, v_\phi)$  plane and compute the normalized residual map, defined as

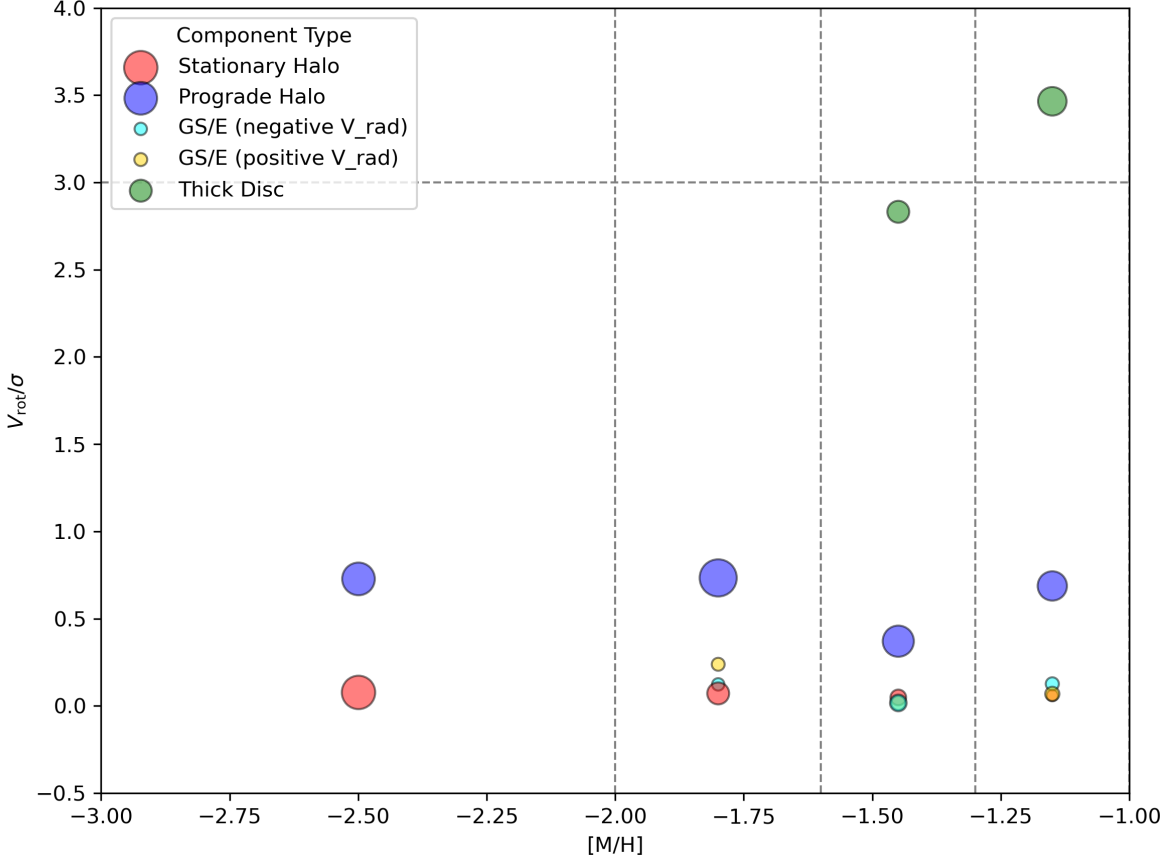


Figure 7: Ratio of mean rotational velocity to azimuthal velocity dispersion,  $V_{\text{rot}}/\sigma_\phi$ , for individual GMM components in each metallicity bin. Larger squares correspond to more dominant components. Colours match the GMM components in Figure 6.(A reproduction of Figure 6 from [Zhang et al. \[2024\]](#))

$$H_{\text{residual}} = \frac{H_{\text{obs}} - H_{\text{mock}}}{H_{\text{obs}} + H_{\text{mock}} + \epsilon},$$

where  $H_{\text{obs}}$  and  $H_{\text{mock}}$  are the 2D histograms and  $\epsilon = 10^{-5}$  is added to avoid division by zero. The residual maps are shown in the top row of Figure 8 for the VMP and IMP bins. The grey dashed ellipses highlight a  $2\sigma$  region of a hypothetical thick disc with mean velocity  $(v_R, v_\phi) = (0, 180)$  km s $^{-1}$  and dispersions  $(\sigma_R, \sigma_\phi) = (70, 50)$  km s $^{-1}$ , consistent with the thick disc component seen in the MP2 metallicity bin.

To quantify the possible presence of a hidden disc, we count the excess number of observed stars inside this thick disc ellipse relative to the GMM-generated sample. We repeat this calculation for 200 Monte Carlo realizations to estimate the residual and its uncertainty. The results are shown as horizontal dashed lines in the bottom row of Figure 8, representing a disc-like residual of  $40.4 \pm 24.8$  stars in the VMP bin and  $76.9 \pm 42.8$  stars in the IMP bin.

To interpret these residuals, we repeat the same procedure but now inject a mock disc population—generated from the same thick disc Gaussian—into the GMM baseline. By varying the injected disc fraction from 0% to 5% of the sample and recalculating

the residual each time, we construct a relationship between disc fraction and expected residual. This is shown as the solid black line in the bottom panels of Figure 8, with the red shaded region indicating the  $1\sigma$  uncertainty across Monte Carlo trials.

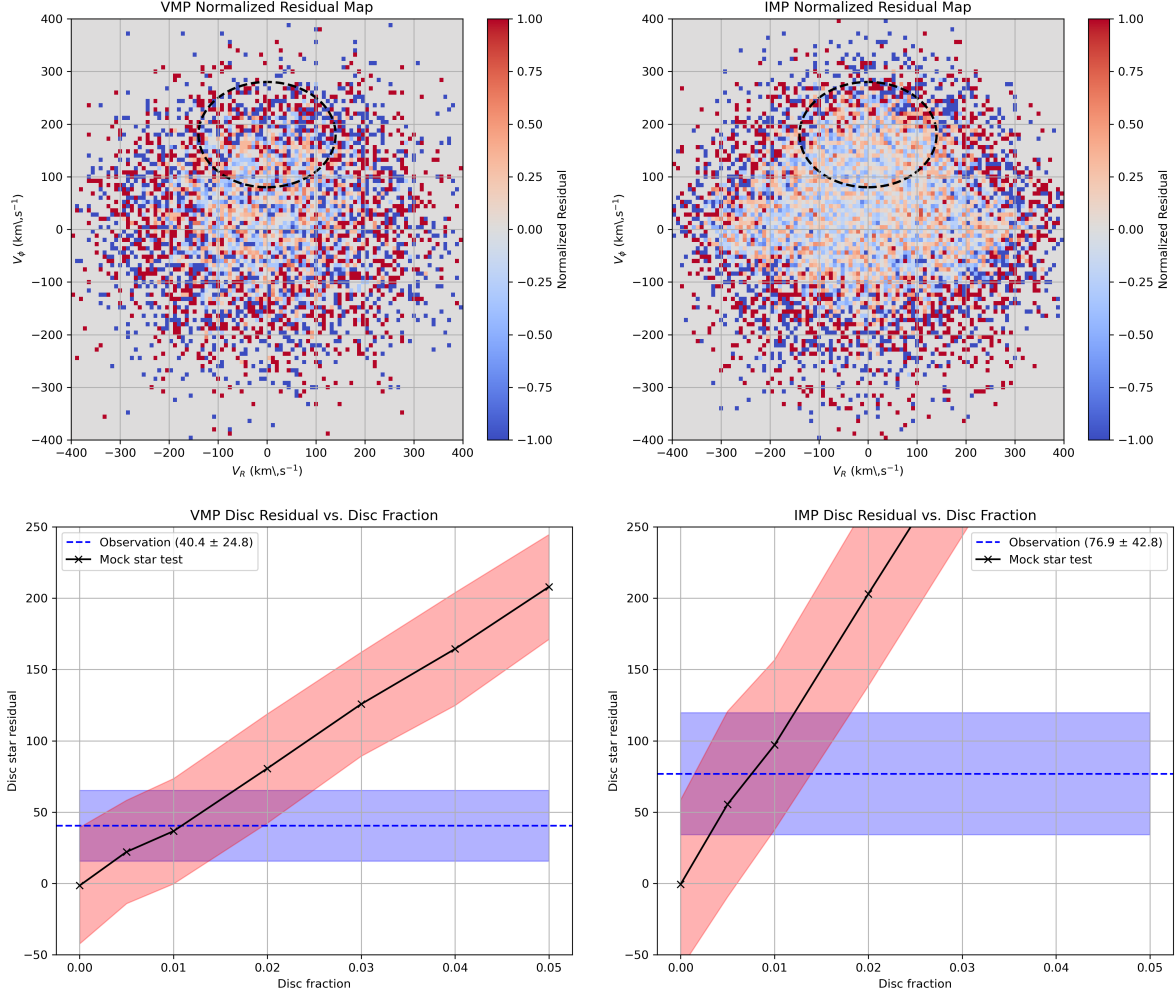


Figure 8: Top: Normalized residual maps between observed and GMM-predicted velocity distributions in  $(v_R, v_\phi)$  for the VMP (left) and IMP (right) metallicity bins. Grey ellipses show the  $2\sigma$  contour of the fiducial thick disc model. Bottom: Disc residuals as a function of injected disc fraction. The dashed line and blue band indicate the observed residual and its uncertainty. The solid black line and red region show mock test results and their uncertainties. (A reproduction of Figure 7 from [Zhang et al. \[2024\]](#))

## 5 Extension analysis

### 5.1 Alpha-element abundance

We extend the chemo-kinematic analysis by adding the alpha-to-iron ratio  $[\alpha/\text{Fe}]$ , where the “alpha” elements (O, Ne, Mg, Si, S, Ca, Ti) are produced almost entirely in core-collapse (Type II) supernovae, whereas most iron is released later by thermonuclear (Type Ia) explosions. Because the two channels operate on very different time-scales— $\sim 10\text{--}30$  Myr for Type II versus  $\gtrsim 0.1\text{--}1$  Gyr for Type Ia—the quantity  $[\alpha/\text{Fe}]$  encodes the star-formation history of a stellar population:

- **High**  $[\alpha/\text{Fe}]$ . Rapid, intense star formation enriches gas with  $\alpha$ -elements before significant iron production from Type Ia supernovae occurs, leading to elevated  $[\alpha/\text{Fe}]$ . This chemical signature is typical of the in-situ thick disc, stellar halo, and some ancient accreted material. However, at fixed metallicity, accreted populations, especially dwarf galaxies, tend to show lower  $[\alpha/\text{Fe}]$  compared to in-situ stars, reflecting their slower chemical evolution.
- **Low**  $[\alpha/\text{Fe}]$ . A more prolonged formation history allowed Type Ia ejecta to accumulate, diluting the alpha enhancement. The present-day thin disc and metal-rich bulge occupy this regime.

Hence the  $[\alpha/\text{Fe}]\text{--}[M/\text{H}]$  plane acts as a chemical clock: populations that overlap in  $[M/\text{H}]$  but differ in formation time-scale separate cleanly in  $[\alpha/\text{Fe}]$ .

Following Viswanathan et al. [2024], we separate the RGB catalogue into high- and low- $[\alpha/\text{M}]$  sequences using the XP abundances of Li et al. [2023] and model each subset with an error-convolved Gaussian-mixture as described earlier. Before fitting the GMM, we can expect to see some differences between the high- and low- $[\alpha/\text{M}]$  sequences as summarised below.

In the high- $[\alpha/\text{M}]$  sequence, the oldest, in-situ population formed rapidly from well-mixed,  $\alpha$ -rich gas. Below  $[M/\text{H}] \approx -1.6$  we therefore expect a single non-rotating halo Gaussian. As enrichment proceeds, gas spins up and produces the thick disc: a prograde, kinematically warm Gaussian whose weight rises steeply between  $[M/\text{H}] \simeq -1.6$  and  $-1.0$  and dominates for  $[M/\text{H}] > -0.7$ . Accreted debris from the last major merger (Gaia–Sausage/Enceladus, GS/E) should not be prominent here because GS/E stars are typically *less*  $\alpha$ -enhanced than the in-situ thick disc at the same metallicity [e.g. Helmi et al., 2018]; our conservative high- $[\alpha/\text{M}]$  cut should remove most of this material.

In the low- $[\alpha/\text{M}]$  sequence, lower  $[\alpha/\text{M}]$  signals slower enrichment, typical of dwarf satellites or the Milky Way disc after Type-Ia supernovae began adding iron. A single halo Gaussian should suffice below  $[M/\text{H}] \approx -1.3$ , with a cold, high-weight thin-disc Gaussian—centred near the Local Standard of Rest and  $\sigma \lesssim 30 \text{ km s}^{-1}$ —emerging above that threshold. Our footprint excludes  $|b| < 10^\circ$ , however, and thus removes most of the geometrically thin disc; the ultra-cold Gaussian may therefore be absent at the low metallicities we are inspecting. The aim is instead to pinpoint the onset of disc-like rotation in the low- $[\alpha/\text{M}]$  sequence despite this selection bias.

## 5.2 Data

We obtain the  $\alpha$ -to-metal abundance ratios from the XP-based catalogue of Li et al. [2023], whose neural-network model, trained on high-resolution APOGEE DR17 spectra, achieves a typical precision of  $\simeq 0.05$  dex for bright sources ( $G < 16$ ). Following Viswanathan et al. [2024], we cross-match the XP-based  $\alpha$  catalogue of Li et al. [2023] with the metallicity-selected red-giant branch sample. This base sample already incorporates the red-giant selection and photometric quality cuts from Andrae et al. [2023], including limits on surface gravity, colour-magnitude position, and XP calibration reliability.

To further ensure robust  $\alpha$  abundances and kinematics, we apply several additional cuts:

- we reject stars within  $1^\circ$  of known dwarf galaxies and those associated with globular clusters;
- a reddening cut  $E(B - V) < 0.5$  removes stars in regions of high extinction, where XP abundances are less reliable;
- a Galactic latitude cut  $|b| > 10^\circ$  similarly avoids the dust-dominated plane;
- we relax the fractional parallax uncertainty cut relative to Section 2.1, requiring only  $f_{\text{pu}} < 0.2$  to retain sufficient stars in the metal-poor regime, which is the focus of this analysis.

We obtain approximately 3.4 million stars in our final sample with alpha element abundances.

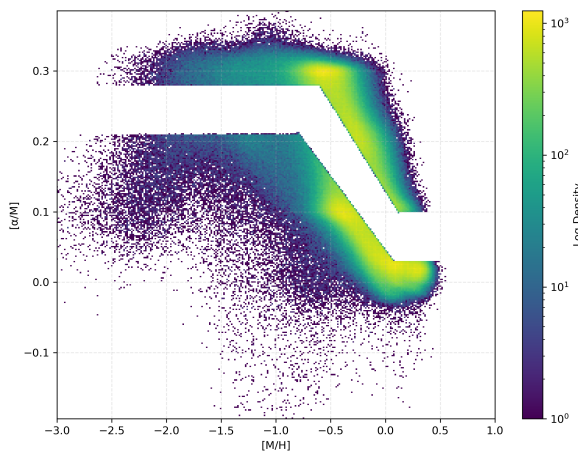


Figure 9: Density of stars in the  $[\alpha/\text{M}]$ – $[\text{M}/\text{H}]$  plane. The high- $\alpha$  and low- $\alpha$  sequences are separated by the piece-wise linear boundary . The transition zone between the two sequences is clearly removed from this plot and discarded from subsequent analysis. (A reproduction of Figure 1 in [Viswanathan et al. \[2024\]](#))

Figure 9 displays the logarithmic density of our RGB sample in the  $[\alpha/\text{M}]$ – $[\text{M}/\text{H}]$  plane. Following [Chandra et al. \[2024\]](#), but with a deliberately tighter boundary as in [Viswanathan et al. \[2024\]](#):

$$\begin{aligned} \text{high-}\alpha : & \begin{cases} [\text{M}/\text{H}] < -0.60 & [\alpha/\text{M}] > 0.28 \\ -0.60 \leq [\text{M}/\text{H}] \leq 0.125 & [\alpha/\text{M}] > -0.25[\text{M}/\text{H}] + 0.13 \\ [\text{M}/\text{H}] > 0.125 & [\alpha/\text{M}] > 0.10 \end{cases} \\ \text{low-}\alpha : & \begin{cases} [\text{M}/\text{H}] < -0.80 & [\alpha/\text{M}] < 0.21 \\ -0.80 \leq [\text{M}/\text{H}] \leq 0.07 & [\alpha/\text{M}] < -0.21[\text{M}/\text{H}] + 0.04 \end{cases} \end{aligned}$$

and discard the intermediate “transition” band.

This high- $\alpha$  threshold is raised so that the chemistry of the Gaia–Sausage/Enceladus debris [[Belokurov et al., 2018](#), [Helmi et al., 2018](#)] does not leak into the in-situ sequence; and the exclusion band is widened to maximise purity in both sub-samples [[Viswanathan et al., 2024](#)].

Figure 10 shows how metallicity varies with Galactocentric radius  $R$  and height  $z$ . The all-star map already hints at a global decline in [M/H] away from the plane and the Solar circle. This decline is more pronounced in the low- $\alpha$  sequence.

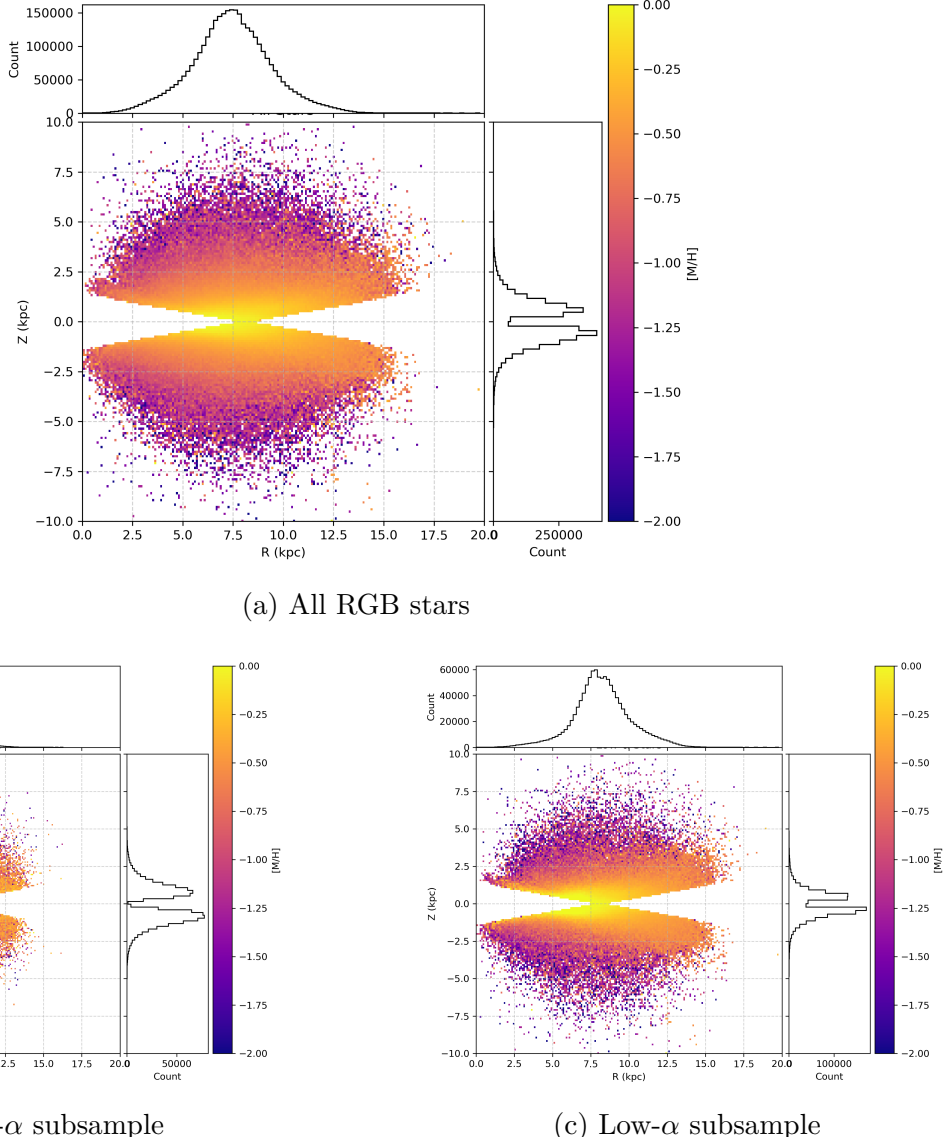


Figure 10: Mean [M/H] colour-coded in the Galactocentric  $R$ - $z$  plane. *Top*: the complete  $G < 16$  RGB sample. *Bottom left*: high- $\alpha$  stars; *bottom right*: low- $\alpha$  stars. The high- $\alpha$  population is more centrally concentrated and shows a shallower vertical metallicity gradient. (A reproduction of Figure 2 in [Viswanathan et al. \[2024\]](#))

As shown in Figure 11, high- $\alpha$  giants exhibit a gradual spin-up with increasing metallicity. At low metallicities ( $[M/H] \lesssim -2$ ), the population shows mild net prograde rotation with large dispersion, consistent with a dynamically hot stellar halo. From  $[M/H] \gtrsim -1.3$ , there is a steady increase in rotation velocity and a corresponding decrease in dispersion, indicative of a transition toward the thick disc. By  $[M/H] \gtrsim -0.5$ , most stars occupy a kinematic regime characterised by elevated  $v_\phi$  and moderate dispersion, consistent with a dynamically hot but rotationally supported thick disc. This continuous trend supports a scenario in which the Galaxy's in-situ population gradually acquired angular momentum

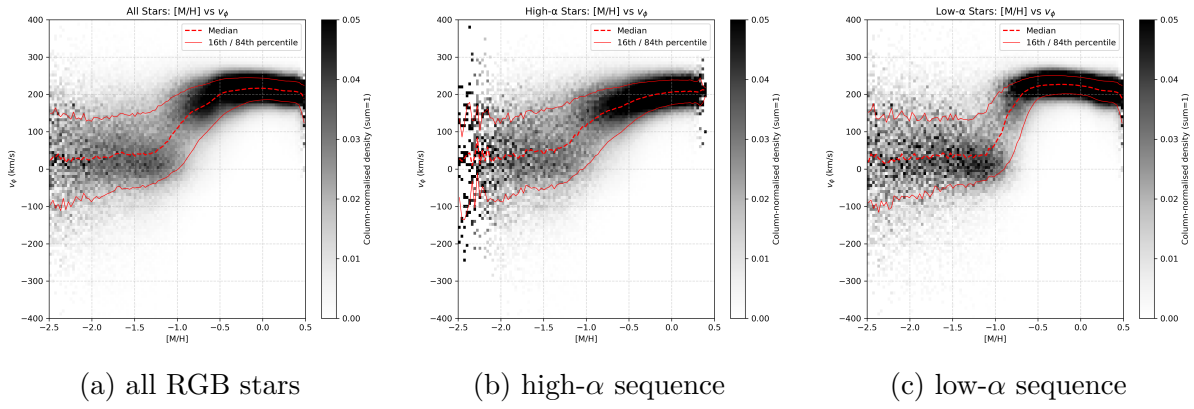


Figure 11: Azimuthal velocity as a function of metallicity. Each panel shows the column-normalised density in the  $[M/H]$ – $v_\phi$  plane together with running medians (red dashed) and 16th/84th percentiles (black). Left: full RGB sample. Centre / right: chemically separated high- $\alpha$  and low- $\alpha$  subsamples. (A reproduction of Figure 3 in [Viswanathan et al. \[2024\]](#))

as star formation progressed.

In the low- $\alpha$  panel, stars with  $[M/H] \lesssim -1.2$  exhibit kinematics similar to those in the high- $\alpha$  sequence, showing mild prograde rotation and high velocity dispersion. However, above  $[M/H] \gtrsim -1.2$ , the low- $\alpha$  sequence undergoes a sharper transition to a population with high net prograde rotation and lower velocity dispersion. By  $[M/H] \gtrsim -0.5$ , the low- $\alpha$  population exhibits kinematics consistent with the thin disc: a strongly rotating, dynamically cold component with lower dispersion than the high- $\alpha$  sequence.

In summary, the high- $\alpha$  sequence shows a gradual transition from a dynamically hot halo to a thick disc, while the low- $\alpha$  sequence shows a more abrupt transition to a dynamically cold disc at higher metallicities.

Following the method described in Section 2.2, we obtain full six-dimensional phase-space coordinates for the chemically separated high- and low- $\alpha$  subsamples. Figure 12 shows the distribution of stars in the  $v_R - v_\phi$  plane across metallicity bins for the high- $\alpha$  (top) and low- $\alpha$  (bottom) populations.

The low- $\alpha$  sample exhibits a strong rotationally supported component, particularly at higher metallicities ( $[\text{M}/\text{H}] \gtrsim -1.0$ ), with a narrow  $v_\phi$  distribution centred around  $\sim 200$  km/s and low radial velocity dispersion—clear hallmarks of thin-disc kinematics. As metallicity decreases, this rotational component becomes less pronounced, with broader distributions in both  $v_R$  and  $v_\phi$  appearing at  $[\text{M}/\text{H}] \lesssim -1.5$ , consistent with increased contamination from halo or accreted populations.

The high- $\alpha$  stars, by contrast, show a continuous transition from a kinematically hot, low-rotation regime at low metallicities to a more rotation-supported disc at higher metallicities. This reflects the gradual build-up of the thick disc over time, as also noted in [Chandra et al. \[2024\]](#). The velocity dispersion is broader throughout, indicating that high- $\alpha$  stars trace older, more dynamically heated populations.

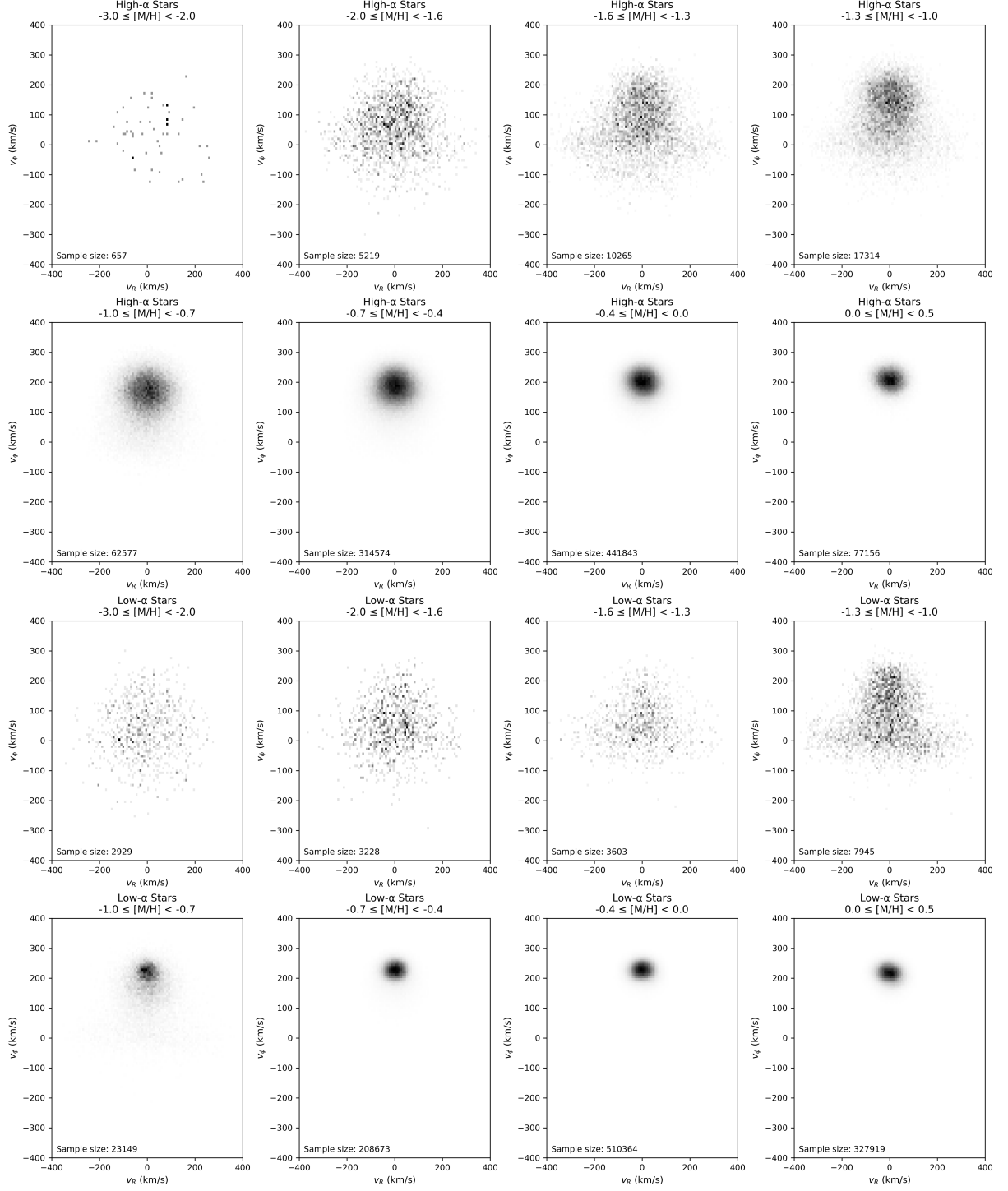


Figure 12: Distribution of stars in  $v_R - v_\phi$  space across eight metallicity bins (increasing left to right, top to bottom) for the high- $\alpha$  population (top) and low- $\alpha$  population (bottom). The low- $\alpha$  stars are clearly more rotation-supported at high metallicities, while the high- $\alpha$  sample shows a broader velocity structure across all bins, consistent with thick-disc and halo populations.

### 5.3 Gaussian Mixture Model Fit

We follow the same Gaussian mixture model fitting procedure as in Section 4.1, but now separately for the high- and low- $\alpha$  sequences.

$\alpha$ -Sequence	VMP ( $[M/H] < -2.0$ )	IMP ( $-2.0 < [M/H] < -1.3$ )	MP1 ( $-1.3 < [M/H] < -1.0$ )	MP2 ( $-1.0 < [M/H] < -0.7$ )
High- $\alpha$	1	4	5	3
Low- $\alpha$	1	2	3	5

Table 2: Number of Gaussian Mixture components selected by the BIC for each metallicity bin, split by  $\alpha$ -sequence.

Following the methodology described in Section 3.2, Table 2 summarises the number of components selected by the Bayesian Information Criterion for each metallicity bin. Detailed BIC scores for each metallicity bin are shown in Figure 13.

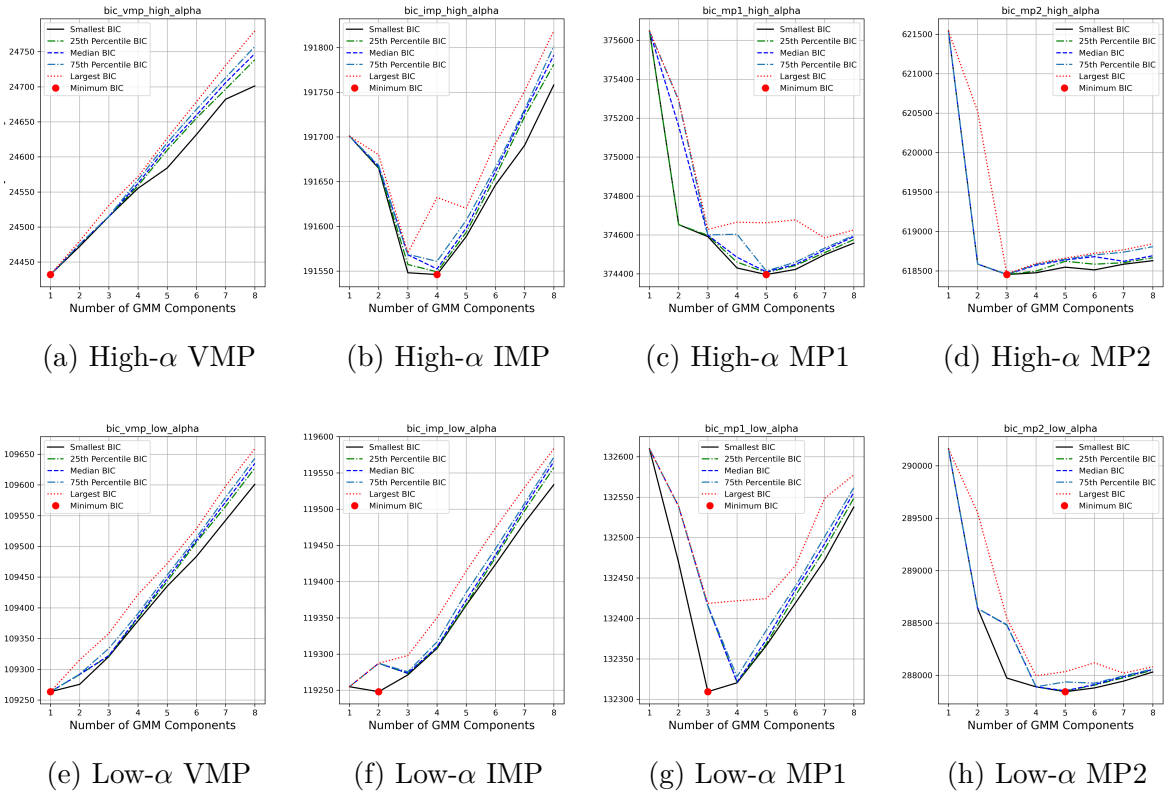


Figure 13: BIC scores for different metallicity bins, grouped by high- and low- $\alpha$  populations.

## 5.4 High alpha Gaussian Mixture Model Fit

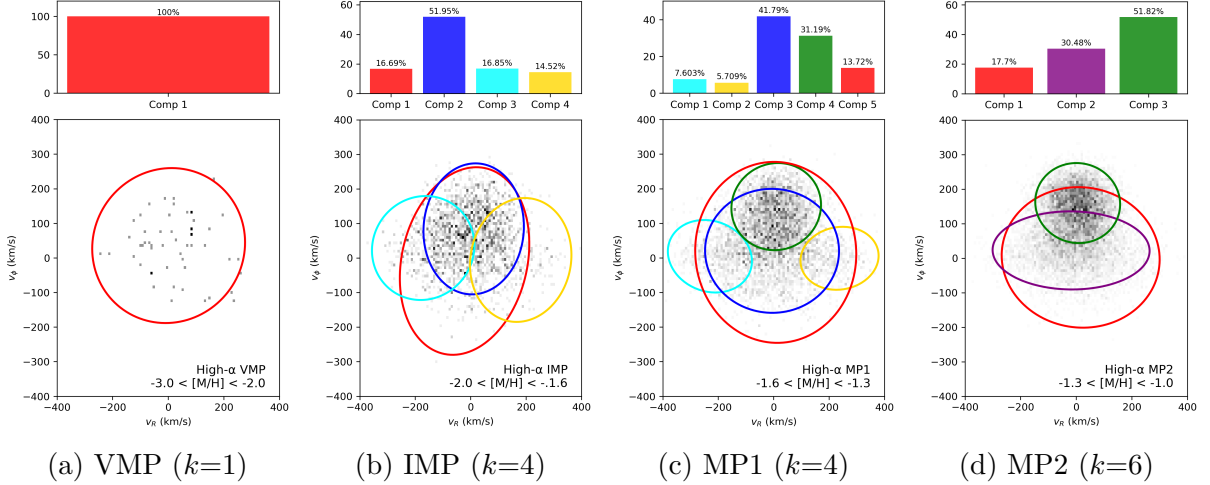


Figure 14: XD-GMM decomposition of high- $\alpha$  giants in four metallicity bins. Grey ellipses mark the  $1\sigma$  contours of each Gaussian component.

Components	Weights (%)	$v_R$	$\sigma_R$	$v_\phi$	$\sigma_\phi$	$v_Z$	$\sigma_Z$
<b>VMP: <math>-3.0 &lt; [M/H] &lt; -2.0</math> (657 stars)</b>							
Stationary halo	100.0	1.40	137.36	35.59	111.99	7.60	102.48
<b>IMP: <math>-2.0 &lt; [M/H] &lt; -1.6</math> (5219 stars)</b>							
Stationary halo	16.7	-22.06	116.74	-8.55	135.74	-2.64	125.40
Prograde halo	51.9	10.84	90.56	84.51	94.79	-0.76	69.42
GS/E (1)	16.8	-171.35	92.33	29.12	75.23	0.50	87.09
GS/E (2)	14.5	180.48	91.48	-5.47	89.66	-2.87	94.37
<b>MP1: <math>-1.6 &lt; [M/H] &lt; -1.3</math> (10265 stars)</b>							
Stationary halo	13.7	7.44	145.24	15.90	130.80	-8.97	127.11
Prograde halo	41.8	-5.85	120.77	20.31	89.59	-1.29	72.85
GS/E (1)	7.6	-230.09	75.81	4.65	52.41	8.69	94.68
GS/E (2)	5.7	237.61	70.43	-1.23	45.51	-3.73	92.81
Thick disc	31.2	9.18	80.79	148.23	62.97	2.99	68.92
<b>MP2: <math>-1.3 &lt; [M/H] &lt; -1.0</math> (17314 stars)</b>							
Stationary halo	17.7	15.91	141.96	2.13	101.75	-1.68	98.90
GS/E	30.5	-18.50	141.08	22.42	56.55	-2.40	77.98
Thick Disk	51.8	5.22	76.27	159.54	57.94	-0.83	67.18

Table 3: GMM component weights and kinematics for the high- $\alpha$  sequence. Velocities are in  $\text{km s}^{-1}$ . Weights indicate the fraction of stars per metallicity bin.

## 5.5 Low alpha Gaussian Mixture Model Fit

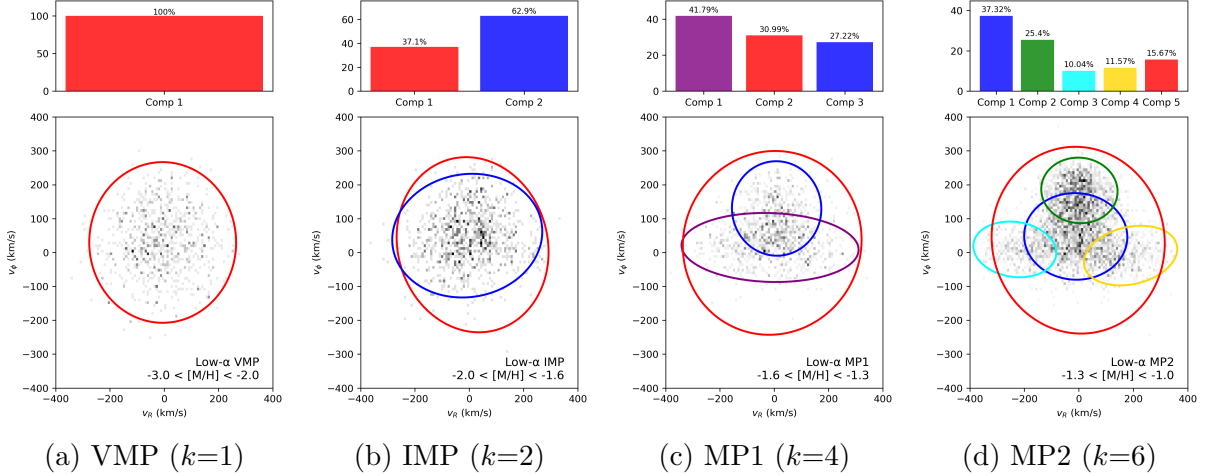


Figure 15: XD–GMM decomposition of low- $\alpha$  giants in four metallicity bins. Grey ellipses show the  $1\sigma$  contours of every Gaussian component.

Components	Weights (%)	$v_R$	$\sigma_R$	$v_\phi$	$\sigma_\phi$	$v_Z$	$\sigma_Z$
<b>VMP: <math>-3.0 &lt; [M/H] &lt; -2.0</math> (2929 stars)</b>							
Stationary halo	100.0	-5.82	135.18	29.55	118.56	1.34	107.10
<b>IMP: <math>-2.0 &lt; [M/H] &lt; -1.6</math> (3228 stars)</b>							
Stationary halo	37.1	12.33	139.85	22.87	129.23	-4.43	120.51
Prograde halo	62.9	-7.34	138.11	49.68	91.25	4.08	75.99
<b>MP1: <math>-1.6 &lt; [M/H] &lt; -1.3</math> (3603 stars)</b>							
Stationary halo	31.0	-7.58	164.57	28.31	135.62	-4.92	121.66
GS/E	41.8	-15.50	162.97	14.71	50.94	-1.93	73.60
Thick Disk/prograde halo	27.2	8.72	82.25	129.87	69.71	3.13	60.68
<b>MP2: <math>-1.3 &lt; [M/H] &lt; -1.0</math> (7945 stars)</b>							
Stationary halo	15.7	-2.30	158.84	36.24	137.81	2.81	131.10
Prograde halo	37.3	-11.31	94.62	47.39	63.89	-1.18	63.12
GS/E (1)	10.0	-234.89	76.09	8.99	41.09	10.70	93.79
GS/E (2)	11.6	189.95	85.58	-9.15	43.99	-8.49	89.69
Thick disc	25.4	2.13	69.98	183.15	48.36	1.75	54.21

Table 4: XD–GMM component weights and kinematics for the low- $\alpha$  sequence. Velocities are in  $\text{km s}^{-1}$ . Weights are the fractional contribution of each component.

## 5.6 Contrasting the high and low $\alpha$ GMMs

The two chemical sequences trace very different roads from a dispersion-supported halo to rotationally supported discs.

**Very-metal-poor regime (VMP;  $[M/H] < -2$ ).** Both data sets are best described by a *single*, non-rotating halo Gaussian. The velocity ellipsoids are close to isotropic ( $\sigma_R : \sigma_\phi : \sigma_Z \approx 1 : 1 : 1$ ), with the high- $\alpha$  stars showing a slightly smaller  $\sigma_\phi$ , hinting at an early prograde bias. Compared to the results in Section 4.1, where two components

were identified in this metallicity regime, the emergence of only a single Gaussian here may reflect the smaller sample size, limiting the ability of the model to resolve multiple distinct halo structures.

**Intermediate regime (IMP;  $-2.0 < [\text{M}/\text{H}] < -1.6$ ).** The low- $\alpha$  sample already splits into stationary and prograde halo Gaussians (37% vs. 63%), whereas the high- $\alpha$  mixture needs *four* hot components, two of which have the highly radial kinematics characteristic of Gaia–Sausage/Enceladus (GSE). The GSE-like signal in the high- $\alpha$  branch is unexpected, as the GSE merger originated from a dwarf galaxy with a slower star formation history and is therefore expected to contribute primarily  $\alpha$ -poor stars. Its appearance here likely reflects mild contamination from  $[\alpha/\text{M}]$  systematics at low signal-to-noise rather than a truly  $\alpha$ -rich GSE population.

**Disc onset (MP1;  $-1.6 < [\text{M}/\text{H}] < -1.3$ ).** In both sequences a prograde component with a low dispersion compatible with a thick disk emerges, but with different prominence and kinematics. In the high- $\alpha$  mixture, the thick disc accounts for 31% of the stars, rotating at  $v_\phi \sim 148 \text{ km s}^{-1}$ , indicating the emergence of a warm, *in-situ* rotating structure. The low- $\alpha$  sample is dominated by non-disc components: the stationary halo and GSE account for 72.8% of the stars, while the remaining 27.2% are captured by a thick-disc/prograde halo Gaussian with  $v_\phi \sim 130 \text{ km s}^{-1}$  and higher dispersions. This suggests that  $\alpha$ -rich stars settled into a disc structure earlier, while  $\alpha$ -poor stars at this metallicity remain primarily associated with accreted debris (GS/E).

**Transition to disc dominance (MP2;  $-1.3 < [\text{M}/\text{H}] < -1.0$ ).** The high- $\alpha$  fit simplifies to three Gaussians—thick disc (52 %), GSE-like halo (31 %), and a small stationary halo (17 %). The low- $\alpha$  solution remains complex (five Gaussians) but now contains a substantial thick disc (25 %) whose lower dispersion ( $\sigma_\phi \sim 48 \text{ km s}^{-1}$ ) and high  $v_\phi$  are consistent with an early thin-disc precursor. The ultra-cold ( $\sigma \lesssim 30 \text{ km s}^{-1}$ ) thin disc is *absent* because our latitude/extinction cuts remove most mid-plane stars.

## 6 Discussion

The discussion of the GMM process mirrors that of the discussion in [Zhang et al. \[2024\]](#). Since the primary goal of this report was to reproduce the results of [Zhang et al. \[2024\]](#), the discussion will focus on the differences between the results of this report and those of [Zhang et al. \[2024\]](#). We do however mention the limitations of the GMM approach and selection effects - which are largely the same as those discussed in [Zhang et al. \[2024\]](#).

### 6.1 Reproducability of [Zhang et al. \[2024\]](#)

The GMM decomposition presented in this report successfully reproduces the same structural features reported by [Zhang et al. \[2024\]](#) by selecting the minimum BIC score for each bin. However, there are several differences in our results worth highlighting.

At the very metal-poor end, our model recovers a nearly even split between stationary and prograde halo components, in contrast to the more dominant non-rotating halo found by [Zhang et al. \[2024\]](#). Although the underlying stellar samples are largely the same, this discrepancy likely reflects the sensitivity of the GMM to initialisation and the precise

kinematic distribution of stars in this low-metallicity regime, where substructure is subtle and overlapping. Notably, the kinematics of the prograde component in our fit are consistent with those reported for Aurora [Belokurov and Kravtsov, 2022], suggesting it may correspond to an early, slightly rotating in-situ population.

In the intermediate metallicity regime ( $-2.0 < [\text{M}/\text{H}] < -1.6$ ), both studies show GSE-like signatures. The agreement in component structure is remarkably consistent, though our fit assigns slightly more weight to the GSE substructures. Interestingly, our GSE components appear with clearer symmetry in radial velocity, which may indicate differences in how the GMM partitions stars with highly eccentric orbits. The recovery of these features in both analyses suggests an ancient radial merger consistent with GS/E [Belokurov et al., 2020].

In the disc onset bin ( $-1.6 < [\text{M}/\text{H}] < -1.3$ ), we find a somewhat higher fraction of thick-disc stars than [Zhang et al. \[2024\]](#), along with slightly lower rotational velocities. This could be due to small variations in how the GMM distinguishes between disc-like and halo-like stars in the transition regime. Despite this, both studies detect a clear emergence of a warm, rotating in-situ component, consistent with the kinematics of a thick disk.

By  $[\text{M}/\text{H}] > -1.3$ , the thick disc becomes a dominant structure in our analysis and that performed by [Zhang et al. \[2024\]](#), almost surpassing the weight of the prograde halo.

In summary, while small discrepancies exist, particularly in the balance between halo and prograde components at low metallicity, there is an overall agreement in results.

We note that we do not attempt to reproduce the action-space analysis of [Zhang et al. \[2024\]](#) in this report. This decision reflects the fact that our analysis focuses on the use of the XD-GMM algorithm, and because of our understanding that orbital actions do not generally follow Gaussian distributions. Unlike velocity space, which can often be approximated as locally Gaussian for distinct stellar populations, action space retains strong imprints of past dynamical processes (e.g. mergers, phase-mixing, resonances) that result in highly non-Gaussian, often multimodal structures.

## 6.2 Expansion of [Viswanathan et al. \[2024\]](#)

We extended the XD-GMM analysis to the high and low  $\alpha$  sequences identified by [Viswanathan et al. \[2024\]](#). Rather than assuming two Gaussian components as in [Viswanathan et al. \[2024\]](#), we fit a Gaussian mixture model with varying numbers of components in each metallicity bin for both sequences. For each case, the optimal number of components was selected based on the minimum BIC score. This allows us to capture the full complexity of the kinematic structure in both sequences, including the presence of multiple halo components and the emergence of thick disc structures at different metallicities.

We were successfully able to reproduce the figures and data preparation described in [Viswanathan et al. \[2024\]](#), as shown in the plots of Section 5.2.

As outlined in Section 5.1, we expected structural differences between the high- and low- $\alpha$  sequences to emerge in the GMM fits. These expectations were largely met: the high- $\alpha$  stars exhibited a clear transition towards a rotationally supported disc at earlier metallicities, while the low- $\alpha$  stars remained halo-dominated until higher metallicities.

One of the more unexpected outcomes of this analysis is the identification of GS/E components within the high- $\alpha$  sequence, despite the GS/E progenitor being associated with a slow star formation history that should result in an  $\alpha$ -poor population. This is likely due to contamination from low signal-to-noise abundance measurements, or challenges in separating overlapping kinematic substructures when using GMMs. In future work, it would be helpful to consider how abundance uncertainties, particularly at low metallicities, may affect the classification of stars. Additionally, as seen in Figure 9, there appears to be a number of low- $\alpha$  stars at  $[M/H] \sim -2.5$  with  $[\alpha/M] \sim 0.1$ . It remains unclear whether this population is real or the result of measurement uncertainties, and it would benefit from further investigation.

### 6.3 Selection Effects and

This part of the discussion closely follows the treatment of selection effects in [Zhang et al. \[2024\]](#). As in their study, our application of quality cuts, such as removing stars with high extinction or low Galactic latitude, and enforcing a strict parallax quality threshold, introduces a non-trivial selection function that affects the relative detectability of different Galactic components.

In particular, the Galactic latitude cut removes many stars near the disc midplane, where the low- $\alpha$  thin disc is most prominent. While relaxing this cut does lead to the identification of a colder, low-dispersion disc component in the low- $\alpha$  sequence at higher metallicities, this component is not considered in our analysis. Our focus is on characterising the onset of disc like kinematics across metallicity in both chemical sequences, rather than describing the well established thin disc. Including low latitude stars would bias the sample toward the disc population, introduce uncertainties in the metallicity estimates, since Gaia XP abundances are known to be less reliable in regions of high extinction, and obscure the halo to disc transition that is central to this investigation.

It is important to note that the component weights derived in this work reflect the properties of our selected sample and should not be generalised to the full Galaxy without modelling the underlying selection function.

### 6.4 Limitations of GMM

Although this part of the discussion mirrors that of [Zhang et al. \[2024\]](#), it is worth reiterating that the Gaussian mixture model approach has several limitations. Gaussian mixtures impose symmetric, ellipsoidal structures in velocity space, which is an oversimplification of the true distribution function of Galactic populations. For instance, the velocity distribution of the thin disc is considered to be non Gaussian due to features such as asymmetric drift, while the GS/E debris has been shown to display bimodal structure in the radial velocity component [[Lancaster et al., 2019](#), [Necib et al., 2019](#)]. In addition, resonant interactions with the Galactic bar may introduce asymmetric and non Gaussian features in the velocity distributions [e.g. [Dillamore et al., 2023](#)].

Following [Zhang et al. \[2024\]](#), we therefore restricted our GMM analysis to the range  $-3 < [M/H] < -1$ , where the thin disc contribution is minimal. At higher metallicities, the GMM attempts to describe the sharp kinematic features of the thin disc using multiple Gaussians, which are not physically meaningful. While more flexible models based on physically motivated distribution functions could better capture these complexities [e.g.

[Binney, 2010](#)], they require significantly more computational effort and are beyond the scope of the aims of both this report and that of [Zhang et al. \[2024\]](#).

Another known limitation of GMMs is their reduced sensitivity to small subpopulations. Like [Zhang et al. \[2024\]](#), we find little evidence for a significant disc like component at low metallicities, but this absence should be interpreted with caution.

## 7 Conclusion

## References

- D. An and T. C. Beers. A blueprint for the milky way’s stellar populations: The power of large photometric and astrometric surveys. *The Astrophysical Journal*, 897(1):39, July 2020. doi: 10.3847/1538-4357/ab8d39. URL <https://ui.adsabs.harvard.edu/abs/2020ApJ...897...39A>.
- F. Anders, P. Gispert, B. Ratcliffe, C. Chiappini, I. Minchev, S. Nepal, A. B. A. Queiroz, J. A. S. Amarante, T. Antoja, G. Casali, L. Casamiquela, A. Khalatyan, A. Miglio, H. Perottoni, and M. Schultheis. Spectroscopic age estimates for apogee red-giant stars: Precise spatial and kinematic trends with age in the galactic disc. *Astronomy and Astrophysics*, 678:A158, Oct. 2023. ISSN 1432-0746. doi: 10.1051/0004-6361/202346666. URL <http://dx.doi.org/10.1051/0004-6361/202346666>.
- R. Andrae, H.-W. Rix, and V. Chandra. Robust data-driven metallicities for 175 million stars from gaia xp spectra. *The Astrophysical Journal Supplement Series*, 267(1):8, jul 2023. doi: 10.3847/1538-4365/acd53e. URL <https://dx.doi.org/10.3847/1538-4365/acd53e>.
- A. Arentsen, E. Starkenburg, N. F. Martin, D. S. Aguado, D. B. Zucker, C. Allende Prieto, V. Hill, K. A. Venn, R. G. Carlberg, J. I. González Hernández, L. I. Mashonkina, J. F. Navarro, R. Sánchez-Janssen, M. Schultheis, G. F. Thomas, K. Youakim, G. F. Lewis, J. D. Simpson, Z. Wan, R. E. Cohen, D. Geisler, and J. E. O’Connell. The pristine inner galaxy survey (pigs) ii: Uncovering the most metal-poor populations in the inner milky way. *Monthly Notices of the Royal Astronomical Society*, 496(4):4964–4978, July 2020a. ISSN 1365-2966. doi: 10.1093/mnras/staa1661. URL <http://dx.doi.org/10.1093/mnras/staa1661>.
- A. Arentsen, E. Starkenburg, N. F. Martin, V. Hill, R. Ibata, A. Kunder, M. Schultheis, K. A. Venn, D. B. Zucker, D. Aguado, R. Carlberg, J. I. González Hernández, C. Lardo, N. Longeard, K. Malhan, J. F. Navarro, R. Sánchez-Janssen, F. Sestito, G. Thomas, K. Youakim, G. F. Lewis, J. D. Simpson, and Z. Wan. The pristine inner galaxy survey (pigs) i: Tracing the kinematics of metal-poor stars in the galactic bulge. *Monthly Notices of the Royal Astronomical Society*, 491(1):L11–L16, January 2020b. doi: 10.1093/mnrasl/slz156. URL <https://ui.adsabs.harvard.edu/abs/2020MNRAS.491L.11A>.
- C. A. L. Bailer-Jones, J. Rybizki, M. Fouesneau, M. Demleitner, and R. Andrae. VizieR Online Data Catalog: Distances to 1.47 billion stars in Gaia EDR3 (Bailer-Jones+, 2021). VizieR On-line Data Catalog: I/352. Originally published in: 2021AJ....161..147B, Feb. 2021.
- V. Belokurov and A. Kravtsov. From dawn till disc: Milky way’s turbulent youth revealed by the apogee+gaia data. *Monthly Notices of the Royal Astronomical Society*, 514(1):689–714, May 2022. ISSN 1365-2966. doi: 10.1093/mnras/stac1267. URL <http://dx.doi.org/10.1093/mnras/stac1267>.
- V. Belokurov, D. Erkal, N. W. Evans, S. E. Koposov, and A. J. Deason. Co-formation of the disc and the stellar halo. *Monthly Notices of the Royal Astronomical Society*, 478(1):611–619, June 2018. ISSN 1365-2966. doi: 10.1093/mnras/sty982. URL <http://dx.doi.org/10.1093/mnras/sty982>.

- V. Belokurov, J. L. Sanders, A. Fattahi, M. C. Smith, A. J. Deason, N. W. Evans, and R. J. J. Grand. The biggest splash. *Monthly Notices of the Royal Astronomical Society*, 494(3):3880–3898, Apr. 2020. ISSN 1365-2966. doi: 10.1093/mnras/staa876. URL <http://dx.doi.org/10.1093/mnras/staa876>.
- J. Binney. Distribution functions for the milky way. *Monthly Notices of the Royal Astronomical Society*, 401(4):2318–2330, Feb. 2010. ISSN 1365-2966. doi: 10.1111/j.1365-2966.2009.15845.x. URL <http://dx.doi.org/10.1111/j.1365-2966.2009.15845.x>.
- S. A. Bird, X.-X. Xue, C. Liu, J. Shen, C. Flynn, C. Yang, G. Zhao, and H.-J. Tian. Constraints on the assembly history of the milky way’s smooth, diffuse stellar halo from the metallicity-dependent, radially dominated velocity anisotropy profiles probed with k giants and bhbs stars using lamost, sdss/segue, and gaia. *The Astrophysical Journal*, 919(1):66, Sept. 2021. ISSN 1538-4357. doi: 10.3847/1538-4357/abfa9e. URL <http://dx.doi.org/10.3847/1538-4357/abfa9e>.
- J. Bland-Hawthorn and O. Gerhard. The galaxy in context: Structural, kinematic, and integrated properties. *Annual Review of Astronomy and Astrophysics*, 54(1):529–596, Sept. 2016. ISSN 1545-4282. doi: 10.1146/annurev-astro-081915-023441. URL <http://dx.doi.org/10.1146/annurev-astro-081915-023441>.
- J. Bovy, D. W. Hogg, and S. T. Roweis. Extreme deconvolution: Inferring complete distribution functions from noisy, heterogeneous and incomplete observations. *The Annals of Applied Statistics*, 5(2B), June 2011. ISSN 1932-6157. doi: 10.1214/10-aoas439. URL <http://dx.doi.org/10.1214/10-AOAS439>.
- J. S. Bullock and M. Boylan-Kolchin. Small-scale challenges to the lambda cdm paradigm. *Annual Review of Astronomy and Astrophysics*, 55(1):343–387, Aug. 2017. ISSN 1545-4282. doi: 10.1146/annurev-astro-091916-055313. URL <http://dx.doi.org/10.1146/annurev-astro-091916-055313>.
- D. Carollo, M. Chiba, M. Ishigaki, K. Freeman, T. C. Beers, Y. S. Lee, P. Tissera, C. Battistini, and F. Primas. Evidence for the third stellar population in the milky way’s disk. *The Astrophysical Journal*, 887(1):22, December 2019. doi: 10.3847/1538-4357/ab517c. URL <https://ui.adsabs.harvard.edu/abs/2019ApJ...887...22C>.
- V. Chandra, V. A. Semenov, H.-W. Rix, C. Conroy, A. Bonaca, R. P. Naidu, R. Andrae, J. Li, and L. Hernquist. The three-phase evolution of the milky way. *The Astrophysical Journal*, 972(1):112, Aug. 2024. ISSN 1538-4357. doi: 10.3847/1538-4357/ad5b60. URL <http://dx.doi.org/10.3847/1538-4357/ad5b60>.
- M. Chiba and T. C. Beers. Kinematics of metal-poor stars in the galaxy. iii. formation of the stellar halo and thick disk as revealed from a large sample of nonkinematically selected stars. *The Astronomical Journal*, 119(6):2843–2865, June 2000. ISSN 0004-6256. doi: 10.1086/301409. URL <http://dx.doi.org/10.1086/301409>.
- G. Cordoni, G. S. Da Costa, D. Yong, A. D. Mackey, A. F. Marino, S. Monty, T. Nordlander, J. E. Norris, M. Asplund, M. S. Bessell, A. R. Casey, A. Frebel, K. Lind, S. J. Murphy, B. P. Schmidt, X. D. Gao, T. Xylakis-Dornbusch, A. M. Amarsi, and A. P. Milone. Exploring the galaxy’s halo and very metal-weak thick disc with skymapper and gaia dr2. *Monthly Notices of the Royal Astronomical Society*, 503

(2):2539–2561, Nov. 2020. ISSN 1365-2966. doi: 10.1093/mnras/staa3417. URL <http://dx.doi.org/10.1093/mnras/staa3417>.

P. Di Matteo, M. Haywood, M. D. Lehnert, D. Katz, S. Khoperskov, O. N. Snaith, A. Gomez, and N. Robichon. The milky way has no in-situ halo other than the heated thick disc: Composition of the stellar halo and age-dating the last significant merger with gaia dr2 and apogee. *Astronomy & Astrophysics*, 632:A4, Nov. 2019. ISSN 1432-0746. doi: 10.1051/0004-6361/201834929. URL <http://dx.doi.org/10.1051/0004-6361/201834929>.

A. M. Dillamore, V. Belokurov, N. W. Evans, and E. Y. Davies. Stellar halo substructure generated by bar resonances. *Monthly Notices of the Royal Astronomical Society*, 524(3):3596–3608, July 2023. ISSN 1365-2966. doi: 10.1093/mnras/stad2136. URL <http://dx.doi.org/10.1093/mnras/stad2136>.

Gaia Collaboration, A. Vallenari, A. G. A. Brown, et al. Gaia data release 3: Summary of the content and survey properties. *Astronomy & Astrophysics*, 674:A1, 2023. doi: 10.1051/0004-6361/202243940.

C. Gallart, E. J. Bernard, C. B. Brook, T. Ruiz-Lara, S. Cassisi, V. Hill, and M. Monelli. Uncovering the birth of the milky way through accurate stellar ages with gaia. *Nature Astronomy*, 3(10):932–939, July 2019. ISSN 2397-3366. doi: 10.1038/s41550-019-0829-5. URL <http://dx.doi.org/10.1038/s41550-019-0829-5>.

D. F. Gray. *The Observation and Analysis of Stellar Photospheres*. Cambridge University Press, 2005.

G. M. Green. dustmaps: A python interface for maps of interstellar dust. *Journal of Open Source Software*, 3(26):695, 2018. doi: 10.21105/joss.00695. URL <https://doi.org/10.21105/joss.00695>.

A. B. Gurvich, J. Stern, C.-A. Faucher-Giguère, P. F. Hopkins, A. Wetzel, J. Moreno, C. C. Hayward, A. J. Richings, and Z. Hafen. Rapid disc settling and the transition from bursty to steady star formation in milky way-mass galaxies. *Monthly Notices of the Royal Astronomical Society*, 519(2):2598–2614, February 2023. doi: 10.1093/mnras/stac3712. URL <https://ui.adsabs.harvard.edu/abs/2023MNRAS.519.2598G>.

M. Haywood, P. Di Matteo, M. D. Lehnert, D. Katz, and A. Gómez. The age structure of stellar populations in the solar vicinity: Clues of a two-phase formation history of the milky way disk. *Astronomy and amp; Astrophysics*, 560:A109, Dec. 2013. ISSN 1432-0746. doi: 10.1051/0004-6361/201321397. URL <http://dx.doi.org/10.1051/0004-6361/201321397>.

A. Helmi. Streams, substructures, and the early history of the milky way. *Annual Review of Astronomy and Astrophysics*, 58(1):205–256, Aug. 2020. ISSN 1545-4282. doi: 10.1146/annurev-astro-032620-021917. URL <http://dx.doi.org/10.1146/annurev-astro-032620-021917>.

A. Helmi and P. Tim de Zeeuw. Mapping the substructure in the galactic halo with the next generation of astrometric satellites. *Monthly Notices of the Royal Astronomical Society*, 319(3):657–665, 2000.

A. Helmi, C. Babusiaux, H. H. Koppelman, D. Massari, J. Veljanoski, and A. G. A.

- Brown. The merger that led to the formation of the milky way’s inner stellar halo and thick disk. *Nature*, 563(7729):85–88, Oct. 2018. ISSN 1476-4687. doi: 10.1038/s41586-018-0625-x. URL <http://dx.doi.org/10.1038/s41586-018-0625-x>.
- L. Lancaster, S. E. Koposov, V. Belokurov, N. W. Evans, and A. J. Deason. The halo’s ancient metal-rich progenitor revealed with bhb stars. *Monthly Notices of the Royal Astronomical Society*, 486(1):378–389, Mar. 2019. ISSN 1365-2966. doi: 10.1093/mnras/stz853. URL <http://dx.doi.org/10.1093/mnras/stz853>.
- H. W. Leung and J. Bovy. Deep learning of multi-element abundances from high-resolution spectroscopic data. *Monthly Notices of the Royal Astronomical Society*, 483(3):3255–3277, 2019.
- J. Li, K. W. K. Wong, D. W. Hogg, H.-W. Rix, and V. Chandra. Aspgap: Augmented stellar parameters and abundances for 23 million rgb stars from gaia xp low-resolution spectra, 2023. URL <https://arxiv.org/abs/2309.14294>.
- M. K. Mardini, A. Frebel, A. Chiti, Y. Meiron, K. V. Brauer, and X. Ou. The atari disk, a metal-poor stellar population in the disk system of the milky way. *The Astrophysical Journal*, 936(1):78, Sept. 2022. ISSN 1538-4357. doi: 10.3847/1538-4357/ac8102. URL <http://dx.doi.org/10.3847/1538-4357/ac8102>.
- P. J. McMillan. The mass distribution and gravitational potential of the milky way. *Monthly Notices of the Royal Astronomical Society*, 465(1):76–94, Oct. 2016. ISSN 1365-2966. doi: 10.1093/mnras/stw2759. URL <http://dx.doi.org/10.1093/mnras/stw2759>.
- P. Melchior and A. Goulding. Filling the gaps: Gaussian mixture models from noisy, truncated or incomplete samples. *Astronomy and Computing*, 25, 11 2016. doi: 10.1016/j.ascom.2018.09.013.
- L. Necib, M. Lisanti, and V. Belokurov. Inferred evidence for dark matter kinematic substructure with sdss–gaia. *The Astrophysical Journal*, 874(1):3, mar 2019. doi: 10.3847/1538-4357/ab095b. URL <https://dx.doi.org/10.3847/1538-4357/ab095b>.
- B. Nordström, M. Mayor, J. Andersen, J. Holmberg, F. Pont, B. R. Jørgensen, E. H. Olsen, S. Udry, and N. Mowlavi. The geneva-copenhagen survey of the solar neighbourhood: Ages, metallicities, and kinematic properties of  $\sim$ 14 000 f and g dwarfs. *Astronomy and Astrophysics*, 418(3):989–1019, Apr. 2004. ISSN 1432-0746. doi: 10.1051/0004-6361:20035959. URL <http://dx.doi.org/10.1051/0004-6361:20035959>.
- J. Norris, M. S. Bessell, and A. J. Pickles. Population studies. i. the bidelman-macconnell “weak-metal” stars. *The Astrophysical Journal Supplement Series*, 58:463–492, July 1985. doi: 10.1086/191049. URL <https://ui.adsabs.harvard.edu/abs/1985ApJS..58..463N>.
- A. B. Pace. The Local Volume Database: a library of the observed properties of nearby dwarf galaxies and star clusters. *arXiv e-prints*, art. arXiv:2411.07424, Nov. 2024. doi: 10.48550/arXiv.2411.07424.
- C. W. Purcell, J. S. Bullock, and A. R. Zentner. Shredded galaxies as the source of diffuse

- intrahalo light on varying scales. *The Astrophysical Journal*, 666(1):20–33, Sept. 2007. ISSN 1538-4357. doi: 10.1086/519787. URL <http://dx.doi.org/10.1086/519787>.
- H.-W. Rix, V. Chandra, R. Andrae, A. M. Price-Whelan, D. H. Weinberg, C. Conroy, M. Fouesneau, D. W. Hogg, F. De Angeli, R. P. Naidu, M. Xiang, and D. Ruz-Mieres. The poor old heart of the milky way. *The Astrophysical Journal*, 941(1):45, Dec. 2022. ISSN 1538-4357. doi: 10.3847/1538-4357/ac9e01. URL <http://dx.doi.org/10.3847/1538-4357/ac9e01>.
- I. B. Santistevan, A. Wetzel, R. E. Sanderson, K. El-Badry, J. Samuel, and C.-A. Faucher-Giguère. The origin of metal-poor stars on prograde disc orbits in fire simulations of milky way-mass galaxies. *Monthly Notices of the Royal Astronomical Society*, 505(1):921–938, July 2021. doi: 10.1093/mnras/stab1345. URL <https://ui.adsabs.harvard.edu/abs/2021MNRAS.505..921S>.
- G. Schwarz. Estimating the dimension of a model. *The Annals of Statistics*, 6(2):461–464, 1978. ISSN 00905364, 21688966. URL <http://www.jstor.org/stable/2958889>.
- R. Schönrich, J. Binney, and W. Dehnen. Local kinematics and the local standard of rest. *Monthly Notices of the Royal Astronomical Society*, 403(4):1829–1833, Apr. 2010. ISSN 1365-2966. doi: 10.1111/j.1365-2966.2010.16253.x. URL <http://dx.doi.org/10.1111/j.1365-2966.2010.16253.x>.
- F. Sestito, N. Martin, and E. Starkenburg. Tracing the formation of the milky way through ultra metal-poor stars. In *The Gaia Universe*, page 47, Apr. 2019. doi: 10.5281/zenodo.3236051.
- F. Sestito, T. Buck, E. Starkenburg, N. F. Martin, J. F. Navarro, K. A. Venn, A. Obreja, P. Jablonka, and A. V. Macciò. Exploring the origin of low-metallicity stars in milky-way-like galaxies with the nihao-uhd simulations. *Monthly Notices of the Royal Astronomical Society*, 500(3):3750–3762, Nov. 2020. ISSN 1365-2966. doi: 10.1093/mnras/staa3479. URL <http://dx.doi.org/10.1093/mnras/staa3479>.
- R. Tkachenko, K. Vieira, A. Lutsenko, V. Korchagin, and G. Carraro. Determining the scale length and height of the milky way’s thick disc using rr lyrae. *Universe*, 11(4):132, apr 2025. doi: 10.3390/universe11040132. URL <http://dx.doi.org/10.3390/universe11040132>.
- K. A. Venn, C. L. Kielty, F. Sestito, E. Starkenburg, N. Martin, D. S. Aguado, A. Aréntsen, P. Bonifacio, E. Caffau, V. Hill, P. Jablonka, C. Lardo, L. Mashonkina, J. F. Navarro, C. Sneden, G. Thomas, K. Youakim, J. I. González-Hernández, R. S. Janssen, R. Carlberg, and K. Malhan. The pristine survey - ix. cfht espadons spectroscopic analysis of 115 bright metal-poor candidate stars. *Monthly Notices of the Royal Astronomical Society*, 492(3):3241–3262, Mar. 2020. doi: 10.1093/mnras/stz3546.
- A. Viswanathan, D. Horta, A. M. Price-Whelan, and E. Starkenburg. A slow spin to win – the gradual evolution of the proto-galaxy to the old disc, 2024. URL <https://arxiv.org/abs/2411.12165>.
- H. Zhang, A. Ardern-Arentsen, and V. Belokurov. On the existence of a very metal-poor disc in the milky way, 2024. URL <https://arxiv.org/abs/2311.09294>.